Article

Applied Spectroscopy

Applied Spectroscopy
0(0) 1–15

DOI: 10.1177/0003702818821330
journals.sagepub.com/home/asp
SAGE

Electrospray Film Deposition for Solvent-Elimination Infrared Spectroscopy

Andrea Arangio[1], Christophe Delval[1,2], Giulia Ruggeri[1,3], Nikunj Dudani[1], Amir Yazdani[1], and Satoshi Takahama[1]

Abstract

The application of electrospray (ES) for quantitative transfer of analytes from solution to an internal reflection element for analysis by attenuated total reflection Fourier transform infrared (ATR FT-IR) spectroscopy has been developed in this work. The ES ATR FT-IR method is evaluated with non-volatile and semi-volatile organic and inorganic compounds dissolved in pure organic solvents or organics in a mixture with water. The technique demonstrates the capability for rapid solvent evaporation from dilute solutions, facilitating the creation of thin films that allow ATR FT-IR to generate transmission-mode-like spectra. Electrospray ATR FT-IR with multiple reflections displays a linear response ($R^2 = 0.95$–0.99) in absorbance with the deposited mass and instrumental detection limit < 100 ng, which demonstrates potential for quantitative applications. The method is applicable when crystalline substances are present, even though the formation of particles restricts the upper limit of mass loadings relative to substances forming homogeneous films. In addition to the solvent, semi-volatile compounds can evaporate during the ES process; the magnitude of losses will depend on solution composition and temperature.

Keywords

Electrospray, infrared spectroscopy, internal reflection, thin films, attenuated total reflection Fourier transform infrared, ATR FT-IR, particulate matter

Date received: 31 August 2018; accepted: 16 November 2018

Introduction

Quantification of substances in solution using Fourier transform infrared (FT-IR) spectroscopy poses formidable challenges on account of IR absorption by the solvent. This task requires restricting the analysis to regions of spectra not affected by the solvent signal or eliminating the solvent altogether. The latter option is especially desirable in multivariate analysis of environmental samples extracted in solution, where maximizing the spectroscopically accessible regions can improve characterization of the unknown (and widely varying) chemical composition. One such application area is in the quantification of molecular structures in atmospheric particulate matter (PM),[1–7] which is a complex mixture of thousands of different types of compounds.[8] Based on absorption bands of vibrational modes, the absolute abundance of organic functional groups or inorganic compounds is reconstructed by spectral analysis of multiple spectral regions simultaneously.[9–17] Furthermore, multiple regions of the spectra are considered simultaneously for factor analysis and source apportionment.[18]

Extensive spectral analysis of PM has thus far been conducted using polytetrafluoroethylene (PTFE) filters, which are sufficiently thin to permit nondestructive, transmission-mode analysis directly, but requires advanced spectral post-processing and imparts interferences that render regions of the spectrum inaccessible. To reduce requirements for statistical post-processing, access more regions of the spectrum, or extend the analysis to other collection substrates, PM can be mechanically transferred to an optically favorable substrate or matrix by pressurization or grinding,[13,17,19–23] but low reproducibility in transfer efficiencies introduce high uncertainties when relating spectra back to the original PM mass loading on the filter. An alternative is to transfer physically the analyte mass by extraction with a controlled volume of solvents, which is also used as a method for polarity separation of chemical

[1]ENAC/IIE Swiss Federal Institute of Technology Lausanne, Lausanne, Switzerland
[2]Current affiliation: European Patent Office, The Hague, Netherlands
[3]Current affiliation: World Health Organization, Geneva, Switzerland

Corresponding author:
Satoshi Takahama, EPFL ENAC IIE APRL, Station 2, CH-1015 Lausanne, Switzerland.
Email: satoshi.takahama@epfl.ch

constituents.[24–27] Therefore, development of a solvent-elimination FT-IR method that is both quantitative in composition and concentration, and at the same time permits relatively high-throughput analysis, is critical to support the growing potential for PM analysis. In particular, low mass loadings of analyte (micrograms) and large solvent volumes (milliliters) required for complete immersion of the collection substrate can lead to high solvent-to-solute ratios in the sample. In this context, we explore capabilities of existing methods and propose a new strategy for solvent-elimination FT-IR that is suitable for PM analysis and for other more general applications. The core concept of solvent elimination is to separate the solute from the solvent by evaporation and to subsequently immobilize it on a substrate before acquiring the FT-IR spectrum.

One of the most reliable quantitative methods of FT-IR spectroscopy is to grind dried sample residues with alkali metal halide powder to create a pellet for transmission-mode analysis.[19] The thickness of these pellets exceeds the wavelength of radiation and therefore can be considered to be equivalent to bulk spectra.[28] Alternatively, the solution containing analytes can be dropped or sprayed into a cup containing a powder matrix (e.g., powder diamond, KBr pellets, or KCl) and analyzed by diffuse reflectance FT-IR (DRIFT).[20,27,29,30] The two methods typically achieve solvent removal by natural convection, heating, and vacuum evaporation during the sample preparation phase, which can take several hours. While the powder matrix preparation procedure is considered to be simpler than the pellet, reproducibility is difficult to achieve with DRIFT on account of homogeneity of the sample coverage, loads, and compactness of the powder layer.[31]

Transmission or reflection–absorption (R/A) analysis can also be applied to dried films formed by direct deposition of solution aliquots onto optically favorable surfaces. Much of this development has been advanced by the liquid chromatography–infrared spectroscopy (LC/IR) community. Aluminum mirrors are commonly used as substrates in R/A spectroscopy because of their compatibility with aqueous solvents but must be handled delicately, and its use can lead to band asymmetry and spectral distortion.[32–34] Better results are obtained with transmission/reflection spectrometry where samples are deposited on IR-transparent optical elements such as KBr and ZnSe windows. Spectra obtained using ZnSe are very close to conventional KBr disk in transmission.[32] Additionally, ZnSe substrates have the advantage of being water-resistant and almost entirely chemically inert (except in highly acidic samples). With all such methods, the flow rate to eliminate organics or aqueous solvents is bound to around 5 μL min^{-1}, mainly because the sample is deposited on a flat surface.[32]

Attenuated total reflectance Fourier transform infrared (ATR FT-IR) spectroscopy is a total internal reflection technique used for studying liquid and solid samples. In ATR FT-IR spectroscopy, incident radiation propagates through the internal reflection element (IRE) via a series of reflections, where a standing wave at each reflection point penetrates and probes the sample. The IR spectrum can be obtained by analyzing the portions of the radiation energy absorbed in this process.[35,36] While commonly used together with fiber optic waveguides or flow-through cells for analysis of solutions,[37,38] the solvent interference can be avoided by depositing a membrane that selectively allows certain analytes to penetrate to the IRE interface.[39] However, when selectivity is not desired, it is also possible to analyze thin films deposited on the surface of an IRE,[40,41] which is the relevant case considered here.

Because optical elements have smooth surfaces, direct sample deposition suffers from heterogeneous films unless the solvent is eliminated efficiently to avoid uncontrolled spreading and uneven drying ("coffee-stain" effect). To alleviate this problem, several techniques have been developed to induce rapid solvent evaporation by spraying off the solution. Thermospray (TSP) is an approach originally developed for LC/MC and further applied to IR spectroscopy.[42] The solution passes through a heated tube where the expanding vapor leads to nebulization of the remaining liquid solution, which is collected on a stainless-steel IR-reflective tape. The working flow rates of TSP are typically in the range of 0.5–1 μL min^{-1} for both organic and aqueous solvents. Although high temperatures used in TSP facilitates liquid throughput and solvent evaporation, they can also cause analyte losses by evaporation or thermal degradation.[32] Particle beams (PB)[43,44] can be generated by nebulizing a solution with helium and removing solvent vaporized in an expansion chamber by momentum separation. The PB approach has strong solvent elimination capacity and a moderately high flow rate (up to 0.3 μL min^{-1}) but the low and variable analyte transfer efficiency (5–10%) limits its applicability for quantification purposes.

Another method developed and successfully applied in mass spectrometry is electrospray (ES) ionization, which was explored for LC/IR analysis by Raynor et al.[45] In ES, a high electrical potential is applied to a needle through which the solution is purged in order to generate a spray of charged micro-droplets. Highly charged micro-droplets break up to form smaller droplets to further facilitate the solvent-elimination with high analyte transfer efficiency, flow rate (1–30 μL min^{-1}), and control. Raynor et al. used a ZnSe plate to collect analytes onto a $\sim$200 μm spot and analyze it by IR microscopy. Promising results were reported along with a recommendation for further investigation on maintaining spray stability for high throughput of solvents with high surface tension (i.e., water). However, development of this method has not been continued to the best of the authors' knowledge.

Electrospray is widely used in many domains: to dissipate liquid samples and ionize samples for mass spectrometry analysis;[46] and to deposit inorganic and polymeric thin films on solid substrate.[47–50] The potential to create thin films

for IR spectroscopy analysis is thus so far underexplored. In the present work, ES is adapted as a solvent elimination strategy to deposit analytes onto a rectangular ZnSe IRE for analysis by multireflection ATR FT-IR spectroscopy in the thin-film limit. The strategy confers capability for rapid evaporation of solvent from micro-droplets and enables to concentrate solutes on the IRE without the need of a solute separation step (e.g., rotary evaporator treatment). Parameters for film deposition, quantitative capability, and film morphology are explored in this work for organic and inorganic compounds dissolved in aqueous and organic solvents.

Attenuated Total Reflection Fourier Transform Infrared Spectroscopy of Thin Films

In the thin film approximation for internal reflection spectroscopy, the electric field can be approximated by the amplitude of the field E_0 at the IRE–sample interface and a linear relation between apparent absorbance A and the physical thickness of the sample can be expected.[35] The concentration of an analyte distributed through this sample mixture can be expressed by an areal density[51] of mass m distributed over area a_N, giving rise to a linear relationship between A and deposited mass m for analyte i (Supplemental Material, Section S1):

$$A = \sum_i \varepsilon_i' m_i \quad \text{where} \quad \varepsilon_i' = \left(\frac{N}{a_N \cos\theta}\right)\left(n_{21} E_0^2\right)\left(\frac{\varepsilon_i}{M_i}\right) \tag{1}$$

N is the number of reflections through a_N, $n_{21} = n_2/n_1$ is the ratio of the real parts of refractive indices of sample medium (n_2) to IRE (n_1), θ is the incident angle, and ε is the molar absorption coefficient. In the definition of the calibration coefficient ε', the first factor in the product is fixed according to the sampling configuration (kept constant for a set of experiments), the second factor is related to the film properties, and the last factor to the target analyte (M is its molar mass). Nominal values for N and a_N based on IRE geometry and θ are used. Equation 1 still applies for less-than-full coverage along the dimension of beam propagation to the extent that the ratio N/a_N computed from nominal values approximates the actual number of reflections through the deposited film per area covered (Supplemental Material, Section S2), though best reproducibility is achieved by covering an identical region of the IRE in each deposition.[52]

n_{21} and E_0 depend on several refractive indices. n_1 is determined by the IRE, for which ZnSe is selected on account of its chemical resistivity and conductivity for serving as a counter electrode. The refractive index n_2 of the multicomponent film may vary according to the sample composition and differ from that of calibration samples. The volume fraction of substances in environmental samples are typically not known a priori, but the contribution of this variation to the absorbance can be small if the overall n_2 of film constituents do not vary substantially.[53] The single-value effective refractive index characterizing the optical behavior of films far thinner than the wavelength of IR[54,55] is bounded by that of its individual components.[56] More representative values may be derived for some anticipated mixture concentrations through effective medium theories (e.g., resistor network models[57,58] or variational principles[59]), but are not considered in the present work and instead included in the calibration coefficient. Another effect of n_2 on the absorbance is imparted by its wavelength dependence — anomalous dispersion near absorption bands can shift the apparent peak location, which is particularly pronounced in the presence of strongly absorbing species.[60,61] However, the assumption of weak absorption (also invoked for Eq. S2) is typically expected to be valid for a wide range of cases,[62] particularly for environmental samples consisting of dilute mixtures. The apparent absorbance and hence the effective thickness $E_0^2 d$ (Supplemental Material, Section S1) for unpolarized radiation, as used in this work, are averages of their contributions from perpendicular and parallel polarizations.[62,63] E_0^2 corresponding to the unpolarized form can therefore be derived from the electric field amplitude normalized by the amplitude of incident radiation[35,64] at the IRE–sample interface for each polarization:

$$E_0^2 = \frac{2\cos^2\theta}{1 - n_{31}^2}\left[1 + \frac{(1 + n_{32}^4)\sin^2\theta - n_{31}^2}{(1 + n_{31}^2)\sin^2\theta - n_{31}^2}\right] \tag{2}$$

The terms $n_{31} = n_3/n_1$ and $n_{32} = n_3/n_2$ reflect the fact that the electric field additionally depends on the refractive index of the substance that lies beyond the film ($n_3 = 1.0$ for air) in the thin film limit. E_0^2 varies inversely with n_2 and their multiplicative product (Eq. 1) dampens the sensitivity of A to n_2, e.g., 10% reduction in n_2 from a nominal value of 1.5 leads to a reduction of only 4% in A. Numerically, the contribution to uncertainty from n_2 in the thin-film approximation is far less than in the more commonly used thick sample limit (where the absorption varies according to $E_0^2 n_2 (n_1^2 \sin^2\theta - n_2^2)^{1/2}$, for which quantitative results have successfully been obtained for other applications.[60,61]

For the multi-reflection ATR hardware considered in this work where a 4 mm-thick ZnSe IRE is used, $\theta = 45^\circ$, $N = 10$, and $n_1 = 2.43$. n_2 for organic compounds vary only within a small range ($n_2 = 1.4$–1.5)[65,66] and are close to inorganic substances, e.g., 1.54 for NaCl, 1.53 for $(NH_4)_2SO_4$, 1.61 for NH_4NO_3, 1.56 for $CaCO_3$, and 1.46 for SiO_2, commonly found in atmospheric particles.[19,67–69] Some additional uncertainty may be introduced through film porosity resulting from the deposition process,

but overall, the dependence of A on variations in n_2 is expected to be small. For this range of refractive indices, the approximate d_p of typical atmospheric PM constituents is 1 μm,[70] with the thin-film approximation applicable for samples in the range of $d = 50–100$ nm.[35]

Thin-Film Deposition Using Electrospray

Attenuated total reflection FT-IR spectral quality and reproducibility are mainly affected by the effective evaporation of solvent, film morphology, and area coverage of the deposition, which are ultimately controlled by droplet size and spray opening. The spray process is governed by hardware geometry (needle size and distance to the collector), ES parameters (applied voltage and liquid feed flow rate), and physical-chemical properties of the sprayed solution (surface tension, dielectric constant, viscosity). While the full process of ES formation, dispersion, and film evolution is difficult to predict even with numerical models, it is possible to obtain some guidance on the operating parameters of the ES based on solvent properties and hardware geometry to evaluate the cone formation requirements, burst rate, and size of the parent droplet.

When a solution is slowly purged through a conductive needle, the liquid is held back in the needle because its surface tension tends to minimize the energy increase due to the enlarged surface. The application of a voltage to the needle enriches the liquid surface with charges that pull the liquid to form an elliptical shape. The shape of the liquid tip results from the balance between electrical forces and liquid surface tension. The ES takes place directly from this liquid tip. While increasing flow rates require increasing voltages to observe a stable spray, the current remains stable within ranges of voltage and flow rate values. These regions are limited by abrupt current changes that indicate the shift towards different working mode where spray droplets have different size.[71–73]

The dripping mode is observed at low voltages when the liquid tip has still an elliptical shape. The mode is characterized by large droplets with uniform size. At constant flow rates, droplet size and emission frequency depend on the applied voltage. Higher voltages decrease the droplet size and increase the emission frequency. Above a certain voltage, the onset voltage V_o, the elliptical shape becomes conical and the solution is pulled to the counter electrode by Coulombic attraction. V_o is determined by several factors related to both solvent properties and instrumental features such as surface tension of the solvent γ_s, needle radius r_n, and distance from the counter electrode d_n. These quantities are related to each other according to the following equation:[74]

$$V_o = A\sqrt{\frac{2\gamma_s r_n \cos\phi_0}{\epsilon_0}}\log\left(\frac{4d_n}{r_n}\right) \quad (3)$$

where ϵ_0 is the dielectric constant in vacuum and ϕ_0 is the half angle of the resulting cone. A is an empirical constant that can be found experimentally and reference values can be found in the literature.[74,75]

Considering an equipotential surface in a static approximation, the cone has a characteristic Taylor angle of 49.3°. In the dynamic case, however, the cone angle is not fixed and varies according to the flow rate of the fluid sprayed.[76] Additionally, if the voltage is not sufficiently high or the flow rate is too high, the cone tip breaks up due to axisymmetric instabilities giving rise to a pulsating mode where the liquid meniscus alternates between a round and conical shape.

Higher voltages stabilize the cone shape to form a liquid filament (jet), giving rise to the single cone-jet mode. In this mode, jet stability and length depend on several parameters such as flow rate, solute concentration, solvent surface tension, and viscosity.[77] The single cone-jet mode is the most studied and commonly used mode in most ES applications, such as mass spectrometry and film deposition. In this mode, it is possible to control key parameters such as molecule ionization efficiency, ion current, droplets size, and film morphology.[78] Further increase of voltage and flow rate gives rise to the multi-jet mode. The cone tip breaks up by forming multiple and smaller jets and their number increases with the applied voltage and flow rate.[71] While the multi-jet mode results in a broader size distribution compared with the cone-jet mode, the resulting smaller droplets[79] (by a factor of three or more, depending on the number of jets) allow more efficient solute-to-solvent separation. Additionally, the higher flow rate required by the multi-jet mode to sustain the ES plays a favorable role in shortening solution deposition times.

We therefore operate in the multi-jet mode for our application. For fixed r_n, d_n, and choice of solvent, the applied voltage is selected such that $V_a > V_o$ (from Eq. 3) where droplet radii fall below the Rayleigh limit and rapidly burst to form a spray plume, with an opening angle proportional to the mass eluted and the number of jets. Smaller droplets and effective evaporation of solvent are generally favored by greater d_n and lower flow rate, or by lower surface tension, lower viscosity, and higher electrical conductivity of the solvent.[80] The particle size affects the drag force which acts against the electrostatic forces, especially that established by the field between needle and counter electrode;[81] the resulting coverage along the long dimension of the IRE has a nonlinear dependence on d_n. Once a suitable condition is found for the ES, multiple parameters are investigated and controlled in order to reduce variability and improve reproducibility among different experimental conditions. The total current is a commonly used parameter to monitor and map the spray stability.[71,79,82] Alternatively, some guidance for operation under different experimental conditions can be found in theoretical estimates of droplet sizes and disintegration times available for the cone-jet mode (Supplemental Material, Section S3).[82–84]

The main principle is to find a set of parameters that results in a similar disintegration time of the initial droplet as the working experiment. Considering that each jet in the multi-jet case is thinner than in the cone-jet mode on account of mass conservation,[79] estimates for the latter can provide upper bounds on the estimated droplet sizes. The variation in voltage required to switch between the two modes may cause variation in actual jet velocities and droplet sizes;[79] therefore, this theory is followed only as a first approximation.

Materials and Methods

Solvent Selection

The choice of solvent must be based on the analytes solubility together with properties which enable stable spray cone generation within not critical conditions for analytes. A critical criterion to obtain stable ES is the surface tension of the solvent. According to Eq. 3, the surface tension, together with needle radius and its distance from the counter electrode, controls the minimum potential required to observe an ES. Solvent permittivity is another important property that needs to be considered in the solvent selection as it determines how efficiently the solution is charged while immersed in the electric field. Solvents with lower permittivity are preferred as their lower capacitance allows rapid charging. Viscosity and vapor pressure are also crucial, as they determine the solvent evaporation time (Eq. S8). In this work, two different solvent solutions were used: pure methanol for organic compounds and methanol : water 5 : 1 in volume for inorganic salts. Table 1 reports values for each property discussed above. Although water is a good solvent for a large variety of inorganic salts and polar organic compounds, its use is not preferred for ES applications. High surface tension and permittivity of water requires the application of large voltages that can cause ozone formation during spray and low vapor pressure make water droplets difficult to evaporates efficiently. Mixtures of water with methanol or ethanol are usually preferred in ES applications.

Electrospray Device

The ES device is built in-house (Supplemental Material, Section S4) and comprises a syringe pump (Fusion 100 - Chemyx, Inc.), 10 mL glass/Teflon syringe (Borosilicatglass - ILS GmbH, Germany), and stainless-steel needle with a diameter of 310 μm (Milian SA). The pump pushes the solution to the needle through a 1 mm i.d. Teflon capillary. The voltage is controlled by means of a National Instrument motherboard (USB X Series 128 channel, National Instruments) and it is further amplified by single output high voltage module (10A12 - UltraVolt, Inc.) to reach kilo-Volt ranges before being applied to the needle. The needle is anchored on a motorized translation stage (MTS50/M-Z8 - 50 mm - Thorlabs, Inc.), mounted all together on a XYZ stage (PT3 - 25 mm, Thorlabs, Inc.), to traverse along the length of the ZnSe crystal ($80 \times 10 \times 4$ mm, 45° - ResulTec). The crystal is held in a polymethylmethacrylate (PMMA) mask anchored on an aluminum board. The entire unit is housed in an enclosed chamber and purged with compressed gas filtered with activated carbon and HEPA capsule (Pall Gelman Corp.). The chamber was maintained at relative humidity (RH) in the range of 6–9% at room temperature (23 °C). The low RH is essential to obtain a stable spray and keep high the evaporation rate and the ionization efficiency.[85]

Electrospray Parameters

Parameters such as voltage V_a, flow rate Q, and distance d_n were found experimentally following the procedure described in the Thin-Film Deposition by Electrospray subsection and are reported in Table 1 . Onset voltages calculated according to Eq. 3 are 3 kV for methanol and 3.5 kV for methanol : water. However, the actual voltage applied V_a was varied up to 5.5 kV for both methanol and methanol : water mixture in order to work under multi-jet spray mode. The upper limit for V_a is determined by the electrochemical stability of the solvent as well as of the species involved in the mixture. Voltages approaching 7 kV are not recommended in air atmosphere as ozone formation takes place in the spray zone.[86,87] For V_a and Q

Table 1. Electrospray solvent characteristics and operating parameters.

Solvent	γ_s (mN m^{-1})	ϵ_0	P_s (kPa)	ρ (g cm^{-3})
MeOH	22.7	32.6	13.0	0.79
MeOH/H_2O	25.5	42.6	26.0	0.84

Solvent	V_a (kV)	Q (μL min^{-1})	d_n (cm)
MeOH	5.5	20–30	1.8
MeOH/H_2O	5.5	9	1.7

MeOH : H_2O denotes a 5 : 1 mixture.
MeOH, methanol.

explored for this study, the minimum acceptable value of d_n is determined experimentally to be about 1 cm; below this distance, droplets of solution are deposited onto the IRE as their travel distance is too short to eliminate the solvent efficiently. With values of Q and d_n reported in Table 1 the resulting droplet disintegration time Δt calculated from Eq. S8 for methanol and methanol : water 5 : 1 mixture were 0.25 and 0.22 μs, respectively. Solute concentrations above the millimolar range cause the plume angle to vary accordingly.[77] In this study, however, the solute concentrations explored are sufficiently low that instrument parameters are robust over a large range of concentrations.

Chemicals

For this work, two organic and two inorganic compounds were selected as standards to test the technique and the related deposition process. Docosanol (1-docosanol, Sigma Aldrich Corp.) is a non-volatile compound with spectroscopically visible aliphatic C-H peaks commonly used for calibration[15,88] and cis-pinonic acid (Sigma Aldrich Corp.) is a semi-volatile reaction product of volatile organic compound oxidation in the atmosphere.[89] Ammonium sulfate and nitrate (Sigma Aldrich Corp.) are inorganic salts commonly found in atmospheric PM.[8] The solutions for organics were prepared using analytical grade methanol (Sigma Aldrich Corp.), whereas inorganic solutions were prepared in a mixture 5 : 1 in volume of methanol and Milli-Q water.

Infrared Spectra

The ZnSe crystal with the deposited material is placed on a HATR crystal plate holder (RCPlate and HATRPlus, PIKE Technologies) and scanned using a Vertex 80 FT-IR spectrometer (Bruker Optics) with deuterated lanthanum α-alanine-doped triglycine sulfate (DLaTGS) detector. Each spectrum is acquired over mid-IR wavenumbers of 4000–400 cm^{-1} as an average of 64 scans. Absorbance spectra are calculated with respect to a clean ZnSe crystal as reference for both stacking experiments, where cumulative aliquots of mass were deposited onto the crystal and single deposition experiment. Transmission spectra were collected on a ZnSe uncoated and flat window (WW71050, Thorlabs Inc.) on which solutions were sprayed by means of a plain-orifice nozzle. The chamber is continuously purged with air treated by a purge-gas generator (Puregas GmbH) to reduce water vapor and carbon dioxide interferences for all scans.

Results and Discussion

Deposition Area

Figure 1 shows the deposition of 50 μg of docosanol on a ZnSe IRE. The deposition was obtained by injecting 0.83 mL of a 60 μg mL^{-1} solution of the compound at a flow rate of 25 mL min^{-1} and applying a voltage of 4.5 kV. Over the IRE surface area of 8 cm^2, the visually detectable area covered by the film is about 6.2 cm^2. Notably, the entire short side of the IRE is homogeneously covered, which is critical to prevent beam filling and achieve quantitative precision.[52,61] As stated above, Eq. 1 still applies in this case of partial coverage along the dimension of beam propagation.

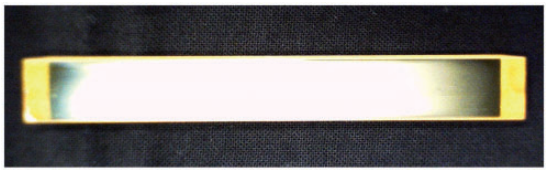

Figure 1. Example of films created by depositing docosanol dissolved in methanol. The visual area covered by the deposition is about 6.2 cm^2. The surface area was estimated algorithmically by image analysis. Pixels in the deposition area were counted and scaled from the IRE size. To enhance the contrast between the deposition area and the background the crystal was illuminated from the top.

Deposition Characterization

Scanning electron microscopy (SEM) images of docosanol and ammonium sulfate depositions are shown in Fig. 2a and b, respectively. As shown in Fig. 2a, ES depositions of docosanol are homogeneous and probably with a low degree of crystallinity. Scanning electron microscopy images of ammonium sulfate depositions (Fig. 2b.i b.ii) reveal that the deposition consists of uniformly dispersed, approximately monodisperse particles with a diameter of 2.0–3.0 μm (Fig. 2b.ii). The formation of particle deposits during the ES process is anticipated by the high apparent crystallinity of ammonium sulfate. The appearance in the images is consistent with nearly spherical geometry of ammonium sulfate crystals (shape factor of 1.02–1.07).[90,91] Scanning electron microscopy images of the mixture docosanol and ammonium sulfate are also reported in Fig. 2c.i and 2c.ii (zoomed in). The film was also obtained by static deposition and encompasses ammonium sulfate particles on an amorphous layer of docosanol. The structure is confirmed by the energy dispersive X-ray (EDX) analysis reported in Fig. 2d where regions in light blue (left) and in red (right) contain mainly nitrogen (denoting ammonium sulfate) and carbon (denoting docosanol), respectively. The formation of crystal deposits is anticipated by thermodynamic preference but can have implications for quantitative analysis by ES ATR FT-IR for several reasons. First, the length scale of heterogeneities in the film approaching that of IR wavelengths invalidates the possibility to consider the packed monolayer as a film with a single refractive index by the effective medium approximation, which makes its optical properties more difficult to interpret. Second, the formation

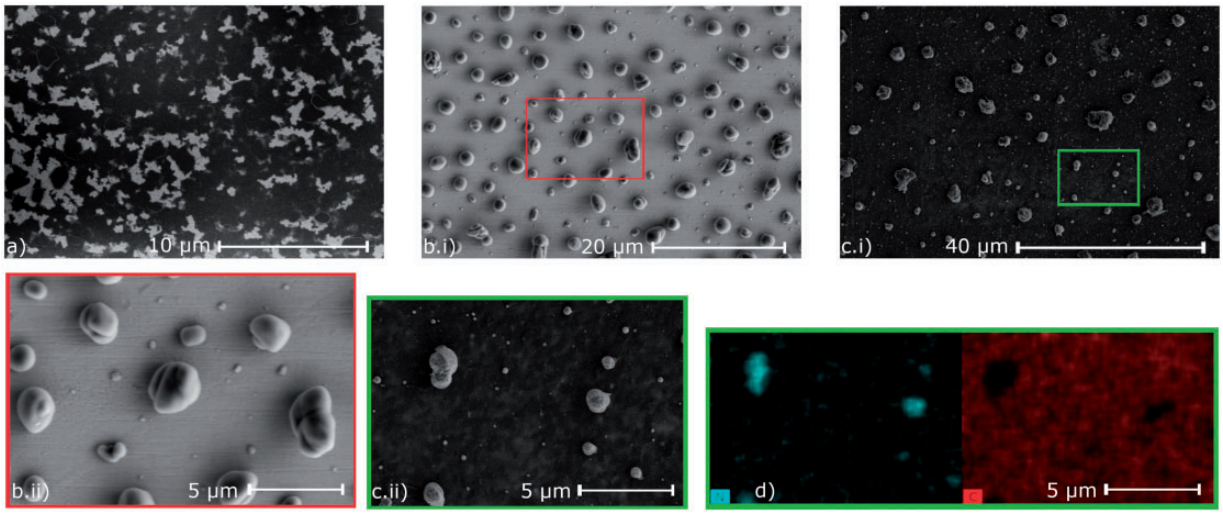

Figure 2. Scanning electron microscopy image of: (a) docosanol deposition on ZnSe; (b.i) ammonium sulfate deposition of ZnSe; (b.ii) zoom-in of b.i; (c.i) docosanol in mixture with ammonium sulfate; (c.ii) zoom-in of c.i; (d) EDX imaging of c.ii for nitrogen in light blue (left side) and carbon in red (right).

of less stable polymorphs of a crystal has been previously reported in ES deposition,[92,93] attributed to Ostwald's rule of stages.[94,95] Given the sensitivity of FT-IR spectroscopy to polymorphic variations,[96] some discrepancies may arise when samples and reference with different crystalline form are compared. Finally, the thin-film regime for ATR FT-IR analysis can be rapidly exceeded when deposited mass is concentrated in particle form. For instance, dense (hexagonal) packing of monodisperse spheres in a plane will lead to a thickness approximately 1.7 times higher than the same mass distributed as a homogeneous film (Supplemental Material, Section S5). Exceedance of the thin-film regime can lead to wavelength-dependent variations in apparent absorbances (Eqs. S2 and S3).

With regards to the last point, the analysis can be kept in a quantitative regime by operating with low mass depositions and controlling the particle film morphology. The deposition of ammonium sulfate shown in Fig. 2 was obtained by spraying the solution continuously in a fixed configuration, without the moving stage operating (depositing 26.9 μg of solute); subsequent analyses are performed with moving stage at lower mass loadings and their spectra are discussed below. An area for future investigation can be to generate droplets with smaller diameter by using slower flow rates and larger V_a/V_o ratio (Eq. S6).

Comparison with Transmission Mode Spectra

In the following section, a qualitative assessment of ATR spectral features of thin films related to several organics (docosanol, cis-pinonic acid, benzoyl peroxide, and azelaic acid) and inorganics such as ammonium sulfate and ammonium nitrate obtained by ES deposition are presented. Fourier transform IR transmission spectra of compounds deposited on ZnSe windows are taken as qualitative reference being this technique a widespread and reliable approach for qualitative FT-IR. Fourier transform IR normalized spectra acquired in transmission (light blue) and in internal reflection mode (orange) are compared in Fig. 3. Overall, ATR spectra present almost identical features compared to transmission spectra, indicating that the application of a high voltage during the ES process does not affect the chemical composition of samples. Attenuated total reflection and transmission spectra for organic compounds present only small differences. In particular, docosanol and cis-pinonic acid in transmission present a slightly higher peak in the region $> 3000\,cm^{-1}$ attributable to –OH functional group probably due to methanol traces still trapped in the deposited film. Azelaic acid and benzoyl peroxide ATR and transmission spectra overlap almost completely over the entire spectral range except for some small differences in the fine structure in the region of 1800–700 cm^{-1}. Spectral overlap is also visible for inorganic compounds investigated and in particular for ammonium sulfate for which both the peak related to N–H stretching $[\nu(NH_4^+)]$ in the region around $3000\,cm^{-1}$ and peaks related to S=O stretching $[\nu(SO_4^{2-})]$ in the $1300\,cm^{-1}$ region present the same features for ATR and transmission spectra in terms of relative absorbance and broadening. For ammonium nitrate, both ATR and transmission spectra display anomalies. The relatively lower absorbance in ATR for the $\nu(NH_4^+)$ band compared to the absorbance in transmission is consistent with exceedances of the thin film limit, which can occur in regimes of lower mass loadings when salt crystals are formed upon deposition (Supplemental Material, S5). The same peak of

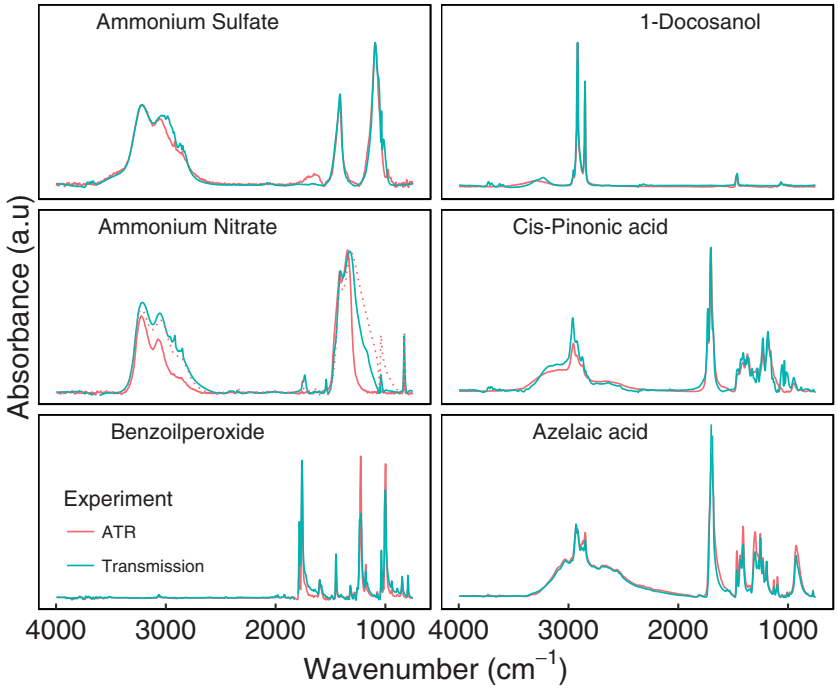

Figure 3. Comparison of FT-IR spectra of the standard compounds acquired in: ATR mode upon deposition with electrospray (orange); transmission mode upon deposition by spray through a plain-orifice nozzle. The ATR spectrum in the dotted line for ammonium nitrate was obtained by spraying the compound solution with a plain-orifice nozzle.

$\nu(NH_4^+)$ in the transmission mode is also affected by the presence of methanol traces from the solvent as visible by the peaks at 2800 cm^{-1}. Additionally, the $\nu(NO_3^-)$ stretch at 1300 cm^{-1} shows an asymmetric broadening towards lower wavenumbers in comparison to literature spectra.[68] An ATR spectrum of ammonium nitrate obtained by spraying with a plain-orifice nozzle is shown for comparison; that it does not display the same wavelength-dependent difference further suggests that the morphology of the electrosprayed film is cause for the difference. With this spectrum, there is a redshift in the 1300 cm^{-1} band due to anomalous dispersion anticipated with high refractive indices.[60] Further investigations into hardware and operating parameters that create favorable morphology by ES deposition for ATR analysis is needed before spectral interpretation and quantitative analysis of samples containing ammonium nitrate can become reliable.

Calibration

Calibration curves and estimates of a test set for docosanol and ammonium sulfate are reported in the following paragraphs. Electrospray depositions allow two different strategies of acquiring ATR spectra. The simplest deposition mode consists into depositing the material onto a clean IRE crystal surface and acquire the IR spectrum of the only sample amount deposited. An alternative deposition mode consists of stacking additional samples of aliquots on top of previous ones and creating a multilayer deposition. The final result is a cumulative spectrum of all aliquots deposited in reference to the clean IRE. The stacking mode allows a more precise evaluation of the thin-film limit assumption by exploring incremental changes in spectra with successive depositions. Figure 4a shows the evolution of the maximum absorbance for the C–H bond stretching of docosanol (band at 2900 cm^{-1}) when aliquots of 4.8 μg are incrementally added and deposited on an IRE with the stacking method. The curve is the result of two sets of experiments where different mass ranges were covered: 0.0–76.8 μg in orange; and 0.0–183.3 μg in green. In both experiments, the absorbance increases linearly within the mass range of 0.0–60.0 μg. In the experiment in orange, the absorbance stays linear up to 76.8 μg. Mass loadings above this point are explored in the experiment in green. Above 100.0 μg, additional mass increments reveal still a linearity with the maximum absorbance but at a lower slope compared to the mass range $<$ 100.0 μg. The nominal film thickness of docosanol calculated assuming a 0.8 g cm^{-3} density[97] and an average surface coverage of 7.2 cm^2 is reported in the top side scale of the plot as reference. In the assumption of a flat and homogeneous film, mass loadings $>$ 60.0 μg have a film thickness $>$ 100 nm. Above this mass loading, the resulting film thickness cannot be neglected in comparison with the penetration depth of the evanescent wave and the electric field of the wave can no longer be considered constant over the film thickness.[35]

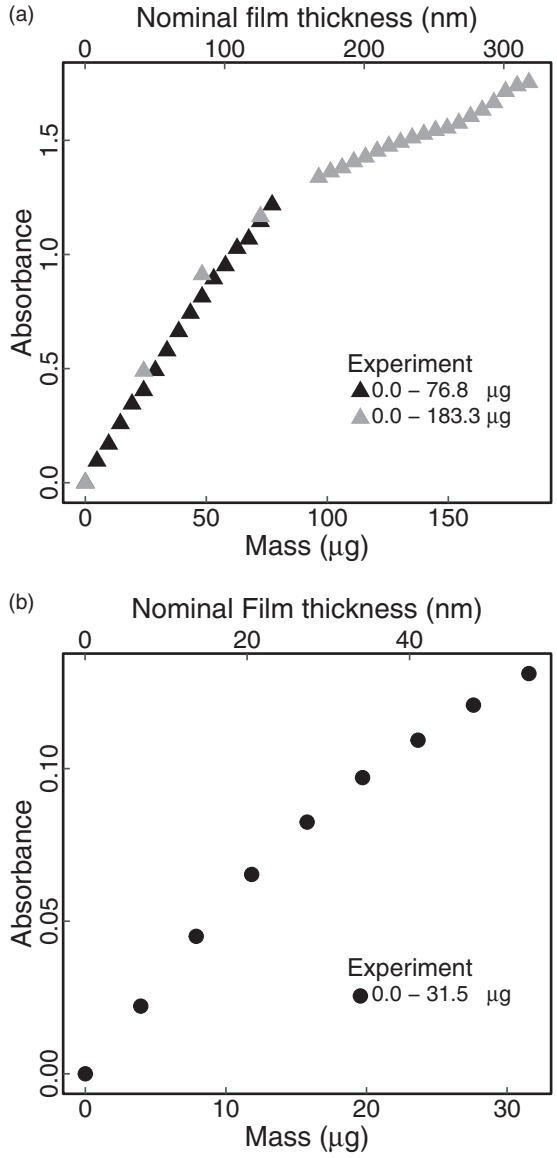

Figure 4. (a) Calibration curve for docosanol (ν(–CH) = 2900 cm^{-1}) obtained by stacking 4.8 μg aliquots from a solution of 60.3 μg mL^{-1} purged at $Q = 20$ μL min^{-1} and $V_a = 4.5$ kV. $R^2 = 0.99$ was obtained considering all points with mass loading < 70 μg; (b) calibration curve for ammonium sulfate ($\nu(SO_4^{2-})$ = 1410 cm^{-1}) obtained by stacking 3.9 μg aliquots from a solution of 49.3 μg mL^{-1} purged at $V_f = 9$ μL min^{-1} and $V_a = 5.5$ kV. A resulting $R^2 = 0.99$ was obtained considering all points with mass loading < 22 μg. The nominal film thickness was calculated by dividing the mass deposited by the estimated areal density of the compound.

Figure 4b shows the evolution of the maximum absorbance for $\nu(SO_4^{2-})$ (band at 1400 cm^{-1}) with mass loading when aliquots of 3.9 μg are incrementally deposited on an IRE using the stacking method. The maximum absorbance varies linearly with respect to the mass loading also for ammonium sulfate but within more restricted mass range than docosanol. The deviation from linearity takes place at mass loadings > 18 μg. Density and refractive index of ammonium sulfate ($\rho = 1.77$ g cm^{-3} and $n_2 = 1.53$) are greater than for docosanol ($\rho = 0.8$ g cm^{-3} and $n_2 = 1.44$ [97]). In the assumption of homogeneous depositions, these two properties should determine for ammonium sulfate more compact films and larger penetration depths implying a larger linearity mass range of the absorbance compared to docosanol. However, as shown in Fig. 2, ammonium sulfate depositions are characterized by particles which diameter grows with the mass loading causing the thin-film approximation to break at lower mass loadings than expected. The first linear portion of the curves reported in Fig. 4 can be used as calibration curve to quantify docosanol and ammonium sulfate in test depositions within the same mass range. To evaluate the quantitative performances of ES ATR FT-IR, the predictions for docosanol and ammonium sulfate are shown in Fig. 5a and 5b, respectively. Test sets for docosanol and ammonium sulfate as pure compounds were composed by varying the deposited volume for the same solution or varying the solution concentration for the same volume of deposition (Supplemental Material, Table S1). In addition to component solutions, a mixture solution containing both docosanol and ammonium sulfate (15.2 and 10.6 μg mL^{-1}, respectively) was also analyzed for evaluation. In contrast to the calibration set, each mass measurement is obtained from the deposition of a single aliquot rather than by sequential layering (stacking). Docosanol was deposited from solutions with concentrations in the range of 6.4–39.1 μg mL^{-1}. Ammonium sulfate was deposited from solutions with concentrations in the range of 10.6–59.3 μg mL^{-1}. The estimated mass (*y*-axes) is in good agreement with the reference value (*x*-axes) for both compounds. The effects of solution concentration on droplet characteristics, deposited mass and deposition procedure (stacking or not) on film morphology, and mixture effects can potentially affect the resulting contact area and refractive index, but they do not appear to affect the performance substantially over the range of conditions studied in these experiments. Furthermore, the spectra of the docosanol and ammonium sulfate mixture is consistent with the expected contributions from its constituents (Supplemental Material, Fig. S5). In general, the deviation in mass estimates is larger for large loadings. In the case of ammonium sulfate, high mass loadings are underestimated because particle formation reduces the suitability of Eq. 1 on which the calibrations are built.

Calibration curves are also used to evaluate the instrumental limit of detection (LOD) which was 1.42 μg of docosanol. Acquiring spectra with a more sensitive liquid nitrogen cooled mercury cadmium telluride (MCT) detector, the LOD for docosanol was estimated to be < 100 ng (Supplemental Material, Section S6). This sensitivity suggests its benefits toward analysis of crystalline compounds at low mass loadings and more generally thin film analysis by ES ATR FT-IR.

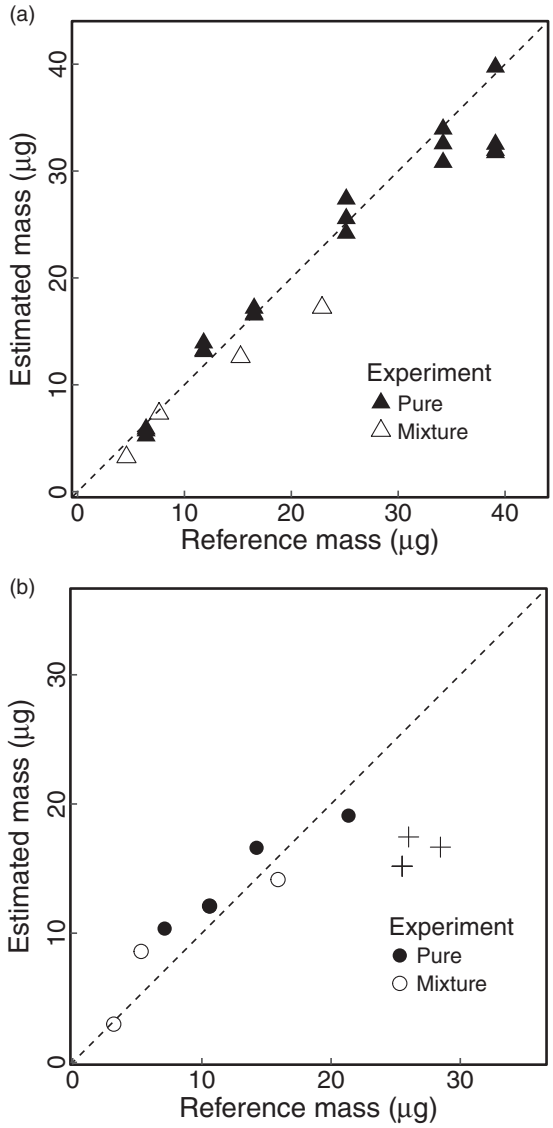

Figure 5. Evaluation of prediction quality for a test set of (a) docosanol (slope = 0.92, $R^2 = 0.99$) and (b) ammonium sulfate (slope = 0.96, $R^2 = 0.95$) depositions from solution with single component (in blue) and in a mixture (orange) of docosanol and ammonium sulfate, respectively. Wavenumbers are same as those used for calibration (Fig. 4). Points in (b) denoted with a cross are not considered in the evaluation as they are out the expected linear regime of calibration (> 21 μg).

Estimates of the Molar Absorption Coefficient

Based on experimental calibration curves and Eqs. 1–2, estimates of ε for docosanol and ammonium sulfate are considered. While there is no comparable reference value for docosanol exists to our knowledge, the estimated value of 1.7×10^5 cm^2 mol^{-1} at 2949 cm^{-1} is in good agreement with the aliphatic C–H stretching absorption coefficients ($2.0–8.0 \times 10^5$ cm^2 mol^{-1}) at the same wavenumber reported for other hydrocarbons in gas and liquid phases.[98–100] For ammonium sulfate, the estimated value of 2.1×10^5 cm^2 mol^{-1} at 1428 cm^{-1} is 53% of the value computed from the imaginary refractive index (Eq. S5) reported at room temperature.[101] The spectra of deposited films are similar to the transmission-mode measurements (Fig. 3) with no strong apparent wavelength-dependent deviations, so it is unlikely that violation of the thin film assumption is the primary cause. Gravimetric analysis of ammonium sulfate electrosprayed onto an aluminum foil covering the IRE indicated that loss of mass outside of the IRE during deposition is not likely. A porous film may lead to lower values of density and n_2 than assumed (for pure substances) due to the presence of air, but plausible deviations from the assumed values and the direction of bias do not account for the difference. However, the approximation for squared electric field amplitude (Eq. 2) may require adjustment[64] for these porous films to relate the apparent absorbance to desired optical constants.

Volatility

Solvent-elimination techniques are best suited for systems where low-volatility compounds are dissolved in highly volatile solvents; retention of solvent and evaporation of semi-volatile compounds are of concern for any analysis technique requiring their separation. Traces of unevaporated solvent can lead to positive bias in quantification, while evaporation of semi-volatile analytes can lead to negative bias. Blank tests of pure methanol revealed that up to 0.1 μg of residual per mL (1.26×10^{-5} %wt) could be detected under the same ES deposition conditions for docosanol. While the solvent residual peak obtained by depositing 4 mL of pure methanol is still six times smaller than the lowest mass loading of docosanol in this study, the influence of this residual should be investigated for each application. Furthermore, solvent residuals in solution may be higher due to a slower evaporation (depression of vapor pressure according to Raoult's law) and additional retention via solute interactions. Environmental samples, including atmospheric PM, can contain semi-volatile compounds that partition between the gas and condensed phase at ambient temperatures. Some fraction of these compounds is lost following typical PM collection protocols, the magnitude of which varies according to sample composition and environmental conditions (e.g., temperature and relative humidity). Losses of semi-volatile organic compounds from filters during sampling have been reported between a few percent to 60% under various conditions,[102–104] while ammonium nitrate losses have been reported in the range of 10–80%.[102,104,105] Nonetheless, quantification of the remaining fraction that is extracted into solution can be hindered by partial evaporation during ES deposition.

To evaluate the extent of such losses, apparent absorbance was recorded for increasing mass loadings of two

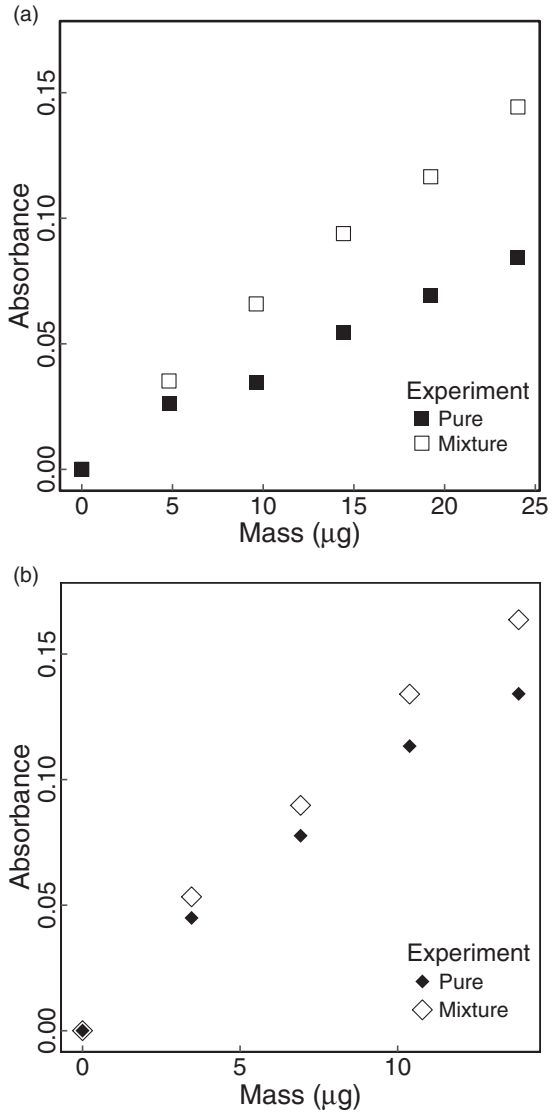

Figure 6. Comparison of the peak absorbance for: (a) cis-pinonic acid (ν(–CO) = 1700 cm^{-1}); and (b) ammonium nitrate ($\nu(NO_3^-)$ = 1340 cm^{-1}) deposited as pure compounds (red) and in mixture (light blue) with docosanol and ammonium sulfate, respectively.

semi-volatile compounds: cis-pinonic acid and ammonium nitrate (Fig. 6). The compounds were electrosprayed from single-solute solutions (cis-pinonic = 30.0 μg mL^{-1}; ammonium nitrate = 17.3 μg mL^{-1}) and from mixtures containing comparable amounts of low-volatility compounds (docosanol = 30.1 μg mL^{-1}; ammonium sulfate = 18.6 μg mL^{-1}). Observed absorbances indicate a systematic increase in mass loading of 100% for cis-pinonic acid and 30% for ammonium nitrate for the deposition of their respective binary-solute mixtures. This difference is attributed to the suppression of volatilization of these semi-volatile species. For this application, the wavelength-dependence of the ammonium nitrate spectrum described previously is not expected to play a substantial role as the absorbance at 1340 cm^{-1} is used for analysis. The vapor pressure for cis-pinonic acid or dissociation constant for ammonium nitrate of the semi-volatile compounds in their ternary solutions (at bulk concentrations) are not lower for either substance compared to their binary solutions;[106–110] the final states after deposition and solvent evaporation should also be the same (solid phase) from the binary and ternary mixture cases[111] (Supplemental Material, Section S8). Therefore, we anticipate that most of the differences observed in Fig. 6 follow initial solvent evaporation and dispersion, when differentiation in droplet composition becomes more pronounced together with the influence of docosanol and ammonium sulfate on the gas/particle partitioning of their semi-volatile counterparts. One strategy for controlling the balance of evaporation of solvent and solute during ES is to control the temperature in the deposition chamber or collection surface. While the deposition plate is often heated in ES film creation to evaporate the residual solvent, this strategy can have an adverse effect on semi-volatile compounds as the enthalpy of vaporization is related to molar volume[112] and is generally smaller for typical solvents than for larger solute molecules. As a first estimate, increasing the temperature from 23 °C to 30 °C will increase the vapor pressure of methanol by 42%, while increasing the vapor pressure of cis-pinonic acid by 113% and dissociation constant of ammonium nitrate by 463%. On the other hand, reducing the temperature from 23 °C to 15 °C will reduce the vapor pressure of methanol by 35% while reducing the vapor pressure of cis-pinonic acid by 60% and ammonium nitrate by 88% (Supplemental Material, S6). This is a strategy that can be further explored if evaporative losses of semi-volatile compounds in the ES process are not sufficiently suppressed by mixture effects, though the possibility of incomplete solvent evaporation may also have to be considered.

Conclusion

A new method for solvent elimination and thin-film deposition onto an optical substrate is proposed in this work. The method, ES ATR FT-IR, demonstrates the separation of solute from a relatively large volume of solution to remove usual interferences caused by the presence of the solvent and takes advantage of the high sensitivity of the ATR FT-IR. Additionally, it is possible to work under the thin-limit assumption which requires no further spectral correction to obtain qualitative and quantitative spectral information. The integration of ATR FT-IR with ES is shown to be reliable for quantification purposes of low-volatility organic (R^2 = 0.99, slope = 0.92) and inorganic compounds (R^2 = 0.95, slope = 0.96) dissolved in both organic solvents or in their mixture with water. The mass range usable for quantification purposes ranges from < 100 ng (using an MCT detector) to 39.1 μg (with DLaTGS detector) for

docosanol, which is deposited as a homogeneous film. Compounds with high crystallinity have a lower upper-limit on mass loading for quantification, as they tend to form heterogeneous and sparse deposits that grow beyond the thin-film regime. Further improvement toward reducing the effect of particle morphology by crystalline compounds may be achieved by increasing the control on deposition morphology through exploration of different needle sizes, distances, voltages, and flow rates. While much of the ES ATR FT-IR characterization for this work was performed with a workhorse DLaTGS detector, the MCT detector may confer advantages for its capability to operate with lower mass loadings of thin films, particularly for cases when restricting the loading is desirable on account of particle-forming compounds present in the sample. We additionally evaluate the retention of semi-volatile compounds, which is generally a challenge with solvent-elimination spectroscopy. When mixed with low-volatility compounds, the mass of semi-volatile deposited compounds increased by 30–100% due to solution effects. Reducing temperatures may also aid in semi-volatile compound retention, though tradeoffs with additional solvent retention may also have to be considered.

Acknowledgments

The authors thank Antoine Wiedmer for help with design of electrospray components, and Pramod Kulkarni and Florian Breider for helpful discussions.

Conflict of Interest

The authors report there are no conflicts of interest.

Funding

This work was funded by the Swiss Federal Office of the Environment (P135-1008), Swiss National Science Foundation (200021_172923), and EPFL.

ORCID iD

Satoshi Takahama http://orcid.org/0000-0002-3335-8741

Supplemental Material

All supplemental material mentioned in the text, consisting of Sections S1–S8, is available in the online version of the journal.

References

1. H. Shaka', N.A. Saliba. "Concentration Measurements and Chemical Composition of PM10-2.5 and PM2.5 at a Coastal Site in Beirut, Lebanon". Atmos. Environ. 2004. 38(4): 523–531.
2. Z. Krivácsy, A. Gelencsér, G. Kiss, et al. "Study on the Chemical Character of Water Soluble Organic Compounds in Fine Atmospheric Aerosol at the Jungfraujoch". J. Atmos. Chem. 2001. 39(3): 235–259.
3. E.R. Graber, Y. Rudich. "Atmospheric HULIS: How Humic-like Are They? A Comprehensive and Critical Review". Atmos. Chem. Phys. 2006. 6(3): 729–753.
4. A. Tiwary, A. Reff, J.J. Colls. "Collection of Ambient Particulate Matter by Porous Vegetation Barriers: Sampling and Characterization Methods". J. Aerosol Sci. 2008. 39(1): 40–47.
5. I. Anil, K. Golcuk, F. Karaca. "ATR-FTIR Spectroscopic Study of Functional Groups in Aerosols: The Contribution of a Saharan Dust Transport to Urban Atmosphere in Istanbul, Turkey". Water Air Soil Pollut. 2014. 225(3): 1898.
6. V. Kumar, A. Goel, P. Rajput. "Compositional and Surface Characterization of HULIS by UV-vis, FTIR, NMR and XPS: Wintertime Study in Northern India". Atmos. Environ. 2017. 164: 468–475.
7. X. Yu, W. Song, Q. Yu, et al. "Fast Screening Compositions of PM 2.5 by ATR-FTIR: Comparison with Results from IC and OC/EC Analyzers". J. Environ. Sci. (China). 2018. 71: 76–88.
8. J. Seinfeld, S. Pandis. Atmospheric Chemistry and Physics: From Air Pollution to Climate Change, 3rd ed. New York, NY: John Wiley & Sons, 2016.
9. Z. Krivácsy, J. Hlavay. "Method for the Reliable Quantitative Analysis by Diffuse Reflectance Infrared Spectroscopy". J. Mol. Struct. 1995. 349: 289–292.
10. D.T. Allen, E.J. Palen, M.I. Haimov, et al. "Fourier Transform Infrared Spectroscopy of Aerosol Collected in a Low Pressure Impactor (LPI/FTIR): Method Development and Field Calibration". Aerosol Sci. Tech. 1994. 21(4): 325–342.
11. S.F. Maria, L.M. Russell, B.J. Turpin, et al. "Source Signatures of Carbon Monoxide and Organic Functional Groups in Asian Pacific Regional Aerosol Characterization Experiment (ACE-Asia) Submicron Aerosol Types". J. Geophys. Res. 2003. 108(D23): 8637.
12. A. Reff, B.J. Turpin, J.H. Offenberg, et al. "A Functional Group Characterization of Organic PM2.5 Exposure: Results from the RIOPA Study. Atmos. Environ. 2007. 41(22): 4585–4598.
13. C. Coury, A.M. Dillner. "A Method to Quantify Organic Functional Groups and Inorganic Compounds in Ambient Aerosols Using Attenuated Total Reflectance FTIR Spectroscopy and Multivariate Chemometric Techniques". Atmos. Environ. 2008. 42(23): 5923–5932.
14. L.M. Russell, S. Takahama, S. Liu, et al. "Oxygenated Fraction and Mass of Organic Aerosol From Direct Emission and Atmospheric Processing Measured on the R/V Ronald Brown During TEXAQS/Gomaccs 2006. J. Geophys. Res. Atmos. 2009. 114D00F05.
15. T.C. Ruthenburg, P.C. Perlin, V. Liu, et al. "Determination of Organic Matter and Organic Matter to Organic Carbon Ratios by Infrared Spectroscopy with Application to Selected Sites in the IMPROVE Network". Atmos. Environ. 2014. 86: 47–57.
16. S. Takahama, A. Johnson, L.M. Russell. "Quantification of Carboxylic and Carbonyl Functional Groups in Organic Aerosol Infrared Absorbance Spectra". Aerosol Sci. Technol. 2013. 47(3): 310–325.
17. P. Faber, F. Drewnick, R. Bierl, et al. "Complementary Online Aerosol Mass Spectrometry and Offline FT-IR Spectroscopy Measurements: Prospects and Challenges for the Analysis of Anthropogenic Aerosol Particle Emissions". Atmos. Environ. 2017. 166: 92–98.
18. S. Takahama, R.E. Schwartz, L.M. Russell, et al. "Organic Functional Groups in Aerosol Particles from Burning and Non-Burning Forest Emissions at a High-Elevation Mountain Site". Atmos. Chem. Phys. 2011. 11(13): 6367–6386.
19. F.E. Volz. "Infrared Refractive Index Of Atmospheric Aerosol Substances". Appl. Opt. 1972. 11(4): 755–759.
20. Z. Krivácsy, J. Hlavay. "Optimization of Sample Packing in Diffuse Reflectance Infrared Spectroscopy". Spectrochim. Acta, Part A. 1994. 50(1): 49–55.
21. P. Veres. FTIR Analysis of Particulate Matter Collected on Teflon Filters in Columbus, OH. [Master's Thesis]. Columbus, OH: Ohio State University, 2005.
22. A. Ghauch, P. Deveau, V. Jacob, et al. "Use of FTIR Spectroscopy Coupled with ATR for the Determination of Atmospheric Compounds". Talanta. 2006. 68(4): 1294–1302.

23. H.M. Hung, Y.Q. Chen, S.T. Martin. "Reactive Aging of Films of Secondary Organic Material Studied by Infrared Spectroscopy". J. Phys. Chem. 2012. 117(1): 108–116.
24. A. Polidori, B.J. Turpin, C.I. Davidson, et al. "Organic PM2.5: Fractionation by Polarity, FTIR Spectroscopy, and OM/OC Ratio for the Pittsburgh Aerosol". Aerosol Sci. Technol. 2008. 42(3): 233–246.
25. R.M. Duarte, A.C. Duarte. "A Critical Review of Advanced Analytical Techniques for Water-Soluble Organic Matter from Atmospheric Aerosols". TrAC: Trends in Analytical Chemistry. 2011. 30(10): 1659–1671.
26. K. Bein, A. Wexler. "A High-Efficiency, Low-Bias Method for Extracting Particulate Matter from Filter and Impactor Substrates". Atmos. Environ. 2014. 90: 87–95.
27. Q. Chen, F. Ikemori, H. Higo, et al. "Chemical Structural Characteristics of HULIS and Other Fractionated Organic Matter in Urban Aerosols: Results from Mass Spectral and FT-IR Analysis". Environ. Sci. Technol. 2016. 50(4): 1721–1730.
28. T. Hasegawa. Quantitative Infrared Spectroscopy for Understanding of a Condensed Matter. Tokyo, Japan: Springer, 2017.
29. R.J. Gordon, N.J. Trivedi, B.P. Singh, et al. "Characterization of Aerosol Organics by Diffuse Reflectance Fourier-Transform Infrared Spectroscopy". Environ. Sci. Technol. 1988. 22(6): 672–677.
30. S.K. Verma, M.K. Deb. "Direct and Rapid Determination of Sulphate in Environmental Samples with Diffuse Reflectance Fourier Transform Infrared Spectroscopy Using Kbr Substrate". Talanta. 2007. 71(4): 1546–1552.
31. G.W. Somsen, T. Visser. "Liquid Chromatography/Infrared Spectroscopy". In: R.A. Meyers, editor. Encyclopedia of Analytical Chemistry. Chichester, UK: John Wiley & Sons, Ltd., 2006.
32. G. Somsen, R. van de Nesse, C. Gooijer, et al. "Spray Jet Assembly Interface for the Coupling of Reversed-Phase Narrow-Bore Liquid Chromatography and Fourier Transform Infrared Spectrometry". J. Chrom. 1991. 552: 635–647.
33. J.J. Gagel, K. Biemann. "Continuous Infrared Spectroscopic Analysis of Isocratic and Gradient Elution Reversed-Phase Liquid Chromatography Separations". Anal. Chem. 1987. 59(9): 1266–1272.
34. R. Fuoco, S.L. Pentoney, P.R. Griffiths. "Comparison of Sampling Techniques for Combined Supercritical Fluid Chromatography and Fourier-Transform Infrared Spectrometry with Mobile Phase Elimination". Anal. Chem. 1989. 61(19): 2212–2218.
35. Harrick NJ. Internal Reflection Spectroscopy. Ossining, NY: Harrick Scientific Corp., 1967.
36. M. Milosevic. Internal Reflection and ATR Spectroscopy. Chemical Analysis. Chichester, UK: John Wiley & Sons, Inc., 2012.
37. J.A. Harrington. Infrared Fibers and Their Applications (SPIE Press Monograph Vol. PM135). Bellingham, WA: SPIE Publications, 2003.
38. A. Urakawa, R. Wirz, T. Bürgi, et al. "ATR-IR Flow-Through Cell for Concentration Modulation Excitation Spectroscopy: Diffusion Experiments and Simulations". J. Phys. Chem. B. 2003. 107(47): 13061–13068.
39. T. Schädle, B. Pejcic, M. Myers, et al. "Fingerprinting Oils in Water Via Their Dissolved VOC Pattern Using Mid-Infrared Sensors". Anal. Chem. 2014. 86(19): 9512–9517.
40. N. Harrick, N. Riederman. "Infrared Spectra of Powders by Means of Internal Reflection Spectroscopy". Spectrochim. Acta. 1965. 21(12): 2135–2139.
41. H.B. Hay, S.C.B. Myneni. "Structural Environments of Carboxyl Groups in Natural Organic Molecules from Terrestrial Systems. Part 1: Infrared Spectroscopy". Geochim. Cosmochim. Acta. 2007. 71(14): 3518–3532.
42. J.A.J. Jansen. On-Line Liquid Chromatography? Fourier Transform Infrared Spectroscopy for the Analysis of Polymers and Additives". Fresenius' Journal of Analytical Chemistry. 1990. 337(4): 398–402.
43. R.M. Robertson, J.A. de Haseth, R.F. Browner. "MAGIC-LC/FT-IR Spectrometry". Microchim. Acta. 1988. 95(1-6): 199–202.
44. R.M. Robertson, J.A. de Haseth, J.D. Kirk, et al. "MAGIC-LC/FT-IR Spectrometry: Preliminary Studies". Appl. Spectrosc. 1988. 42(8): 1365–1368.
45. M.W. Raynor, K.D. Bartle, B.W. Cook. "Electrospray Micro Liquid Chromatography-Fourier Transform Infrared Micro Spectrometry". J. Separ. Sci. 1992. 15(6): 361–366.
46. M. Wilm. "Principles of Electrospray Ionization". Mol. Cell. Proteomics. 2011. 10(7): M111.009407.
47. H. Tang, C. Yang, Z. Lin, et al. "Electrospray-Deposition of Graphene Electrodes: A Simple Technique to Build High-Performance Supercapacitors". Nanoscale. 2015. 7(20): 9133–9139.
48. A. Jaworek. "Electrospray Droplet Sources for Thin Film Deposition". J. Mater. Sci. 2006. 42(1): 266–297.
49. W. Hwang, G. Xin, M. Cho, et al. "Electrospray Deposition of Polymer Thin Films for Organic Light-Emitting Diodes". Nanoscale Res. Lett. 2012. 7(1): 52.
50. N.A. Brown, J.N. Gladstone, P.R. Chiarot. "Evolution of Nanoparticle Deposits Printed Using Electrospray". Journal of Micro and Nano-Manufacturing. 2014. 3(1): 014502.
51. A.W. Adamson. A Textbook of Physical Chemistry, 2nd ed. New York: Academic Press, 1979.
52. ASTM International. Practices for Internal Reflection Spectroscopy. Available at: https://doi.org/10.1520/E0573-01R13.
53. B.C. Smith. Fundamentals of Fourier Transform Infrared Spectroscopy, 2nd ed. Boca Raton, FL: CRC Press, 2011.
54. G.A. Niklasson, C.G. Granqvist, O. Hunderi. "Effective Medium Models for the Optical Properties of Inhomogeneous Materials". Appl. Opt. 1981. 20(1): 26–30.
55. T.C. Choy. Effective Medium Theory: Principles and Applications, 2nd ed. Oxford: Oxford University Press, 2016.
56. R.J. Gehr, R.W. Boyd. "Optical Properties of Nanostructured Optical Materials. Chem. Mater. 1996. 8(8): 1807–1819.
57. O. Wiener. "Zur theorie der refraktionskonstanten. Berichte über die Verhandlungen der Königlich-Sächsischen Gesellsschaft der Wissenschaften zu Leipzig. 1910. 62: 256–277.
58. G.W. Milton. Bounds on the Complex Permittivity of a Two-Component Composite Material". J. Appl. Phys. 1981. 52(8): 5286–5293.
59. Z. Hashin, S. Shtrikman. "A Variational Approach to the Theory of the Effective Magnetic Permeability of Multiphase Materials". J. Appl. Phys. 1962. 33(10): 3125–3131.
60. G. Ramer, B. Lendl. "Attenuated Total Reflection Fourier Transform Infrared Spectroscopy". In: R.A. Meyers (ed.) Encyclopedia of Analytical Chemistry. Chichester, UK: John Wiley & Sons, Ltd., 2006.
61. P.R. Griffiths, J.A. De Haseth. Fourier Transform Infrared Spectrometry. Hoboken, NJ: Wiley-Interscience, 2007.
62. F.M. Mirabella. "Principles, Theory and Practice of Internal Reflection Spectroscopy". In: J.M. Chalmers, P.R. Griffiths, editors. Handbook of Vibrational Spectroscopy. Chichester, UK: John Wiley & Sons, Ltd., 2006.
63. T.D. Tickanen, M.I. Tejedor-Tejedor, M.A. Anderson. "Quantitative Characterization of Aqueous Suspensions Using Attenuated Total Reflection Fourier Transform Infrared Spectroscopy: Influence of Internal Reflection Element-Particle Interactions on Spectral Absorbance Values". Langmuir. 1991. 7(3): 451–456.
64. P.H. Axelsen, M.J. Citra. "Orientational Order Determination by Internal Reflection Infrared Spectroscopy". Prog. Biophys. Mol. Biol. 1996. 66(3): 227 – 253.
65. M.L. Smith, M. Kuwata, S.T. Martin. "Secondary Organic Material Produced by the Dark Ozonolysis of A-Pinene Minimally Affects the Deliquescence and Efflorescence of Ammonium Sulfate". Aerosol Sci. Technol. 2011. 45(2): 244–261.
66. K. Li, J. Li, W. Wang, et al. "Effects of Gas-Particle Partitioning on Refractive Index and Chemical Composition of M-Xylene Secondary Organic Aerosol". J. Phys. Chem. 2018. 122(12): 3250–3260.

67. O.B. Toon, J.B. Pollack, B.N. Khare. "The Optical Constants of Several Atmospheric Aerosol Species: Ammonium Sulfate, Aluminum Oxide, and Sodium Chloride". J. Geophys. Res. 1976. 81(33): 5733–5748.
68. M.A. Jarzembski, M.L. Norman, K.A. Fuller, et al. "Complex Refractive Index of Ammonium Nitrate in the 2–20μm Spectral Range". Appl. Opt. 2003. 42(6): 922–930.
69. W. Wang, M.J. Rood. "Real Refractive Index: Dependence on Relative Humidity and Solute Composition with Relevancy to Atmospheric Aerosol Particles". J. Geophys. Res. 2008. 113(D23): D23305.
70. D.T. Allen, E. Palen. "Recent Advances in Aerosol Analysis by Infrared Spectroscopy". J. Aerosol Sci. 1989. 20(4): 441–455.
71. C. Ryan, K. Smith, J. Stark. "Characterization of Multi-Jet Electrospray Systems". J. Aerosol Sci. 2012. 51: 35–48.
72. P.R. Chen, D.Y. Pui, S.L. Kaufman. "Electrospraying of Conducting Liquids for Monodisperse Aerosol Generation in the 4 nm to 1.8 μm Diameter Range". J. Aerosol Sci. 1995. 26(6): 963–977.
73. M. Cloupeau, B. Prunet-Foch. "Electrohydrodynamic Spraying Functioning Modes: A Critical Review". J. Aerosol Sci. 1994. 25(6): 1021–1036.
74. D.P. Smith. "The Electrohydrodynamic Atomization of Liquids". IEEE Transactions on Industry Applications. 1986. IA-22(3): 527–535.
75. A.R. Jones, K.C. Thong. "The Production of Charged Monodisperse Fuel Droplets by Electrical Dispersion". J. Phys. Appl. Phys. 1971. 4(8): 1159–1166.
76. J.F. De La Mora. "The Effect of Charge Emission from Electrified Liquid Cones". J. Fluid Mech. 1992. 243: 561.
77. Y. Wang, M.K. Tan, D.B. Go, et al. "Electrospray Cone-Jet Breakup and Droplet Production for Electrolyte Solutions". Europhys. Lett. 2012. 99(6): 64003.
78. I.B. Rietveld, K. Kobayashi, H. Yamada, et al. "Electrospray Deposition, Model, and Experiment: Toward General Control of Film Morphology". J. Phys. Chem. 2006. 110: 23351–23364.
79. P.D. Noymer, M. Garel. "Stability and Atomization Characteristics of Electrohydrodynamic Jets in the Cone-Jet and Multi-Jet Modes". J. Aerosol Sci. 2000. 31(10): 1165–1172.
80. J.A. Tapia-Hernández, P.I. Torres-Chávez, B. Ramírez-Wong, et al. "Micro- and Nanoparticles by Electrospray: Advances and Applications in Foods. J. Agr. Food Chem. 2015. 63(19): 4699–4707.
81. K. Tang, A. Gomez. "On the Structure of an Electrostatic Spray of Monodisperse Droplets". Phys. Fluid. 1994. 6(7): 2317–2332.
82. L. Tang, P. Kebarle. "Dependence of Ion Intensity in Electrospray Mass Spectrometry on the Concentration of the Analytes in the Electrosprayed Solution". Anal. Chem. 1993. 65(24): 3654–3668.
83. M.S. Wilm, M. Mann. "Electrospray and Taylor-Cone Theory, Dole's Beam of Macromolecules at Last?". Int. J. Mass Spectrom. Ion Process. 1994. 136(2): 167–180.
84. A. Gomez, K. Tang. "Charge and Fission of Droplets in Electrostatic Sprays". Phys. Fluids. 1994. 6(1): 404–414.
85. S. Nguyen, J.B. Fenn. "Gas-Phase Ions of Solute Species from Charged Droplets of Solutions". Proc. Natl. Acad. Sci. 2007. 104(4): 1111–1117.
86. X. Yan, R.M. Bain, R.G. Cooks. "Organic Reactions in Microdroplets: Reaction Acceleration Revealed by Mass Spectrometry". Angew. Chem. Int. Ed. 2016. 55(42): 12960–12972.
87. S. Banerjee, E. Gnanamani, X. Yan, et al. "Can All Bulk-Phase Reactions Be Accelerated in Microdroplets?". The Analyst. 2017. 142(9): 1399–1402.
88. S. Gilardoni, L.M. Russell, A. Sorooshian, et al. "Regional Variation of Organic Functional Groups in Aerosol Particles on Four US East Coast Platforms During the International Consortium for Atmospheric Research on Transport and Transformation 2004 Campaign. J. Geophys. Res. Atmos. 2007. 112(D10): D10S27.
89. J.Z. Yu, D.R. Cocker, R.J. Griffin, et al. "Gas-Phase Ozone Oxidation of Monoterpenes: Gaseous and Particulate Products". J. Atmos. Chem. 1999. 34(2): 207–258.
90. G. Biskos, D. Paulsen, L.M. Russell, et al. "Prompt Deliquescence and Efflorescence of Aerosol Nanoparticles". Atmos. Chem. Phys. 2006. 6: 4633–4642.
91. A. Zelenyuk, Y. Cai, D. Imre. "From Agglomerates of Spheres to Irregularly Shaped Particles: Determination of Dynamic Shape Factors from Measurements of Mobility and Vacuum Aerodynamic Diameters". Aerosol Sci. Technol. 2006. 40(3): 197–217.
92. J. Sakata, M. Mochizuki. "Preparation of Organic Thin Films by an Electrospray Technique I. Crystal Forms and Their Orientation in Poly(Vinylidene Flouride) Films". Thin Solid Films. 1991. 195(1): 175 – 184.
93. M. Wang, G.C. Rutledge, A.S. Myerson, et al. "Production and Characterization of Carbamazepine Nanocrystals by Electrospraying for Continuous Pharmaceutical Manufacturing". J. Pharm. Sci. 2012. 101(3): 1178–1188.
94. W. Ostwald. "Studien über die bildung und umwandlung fester körper". Zeitschrift für Physikalische Chemie. 1897. 22U: 289.
95. T. Threlfall. "Structural and Thermodynamic Explanations of Ostwald's Rule". Org. Process Res. Dev. 2003. 7(6): 1017–1027.
96. H.B. Wu, M.N. Chan, C.K. Chan. FTIR Characterization of Polymorphic Transformation of Ammonium Nitrate". Aerosol Sci. Technol. 2007. 41(6): 581–588.
97. D.R. Lide, G. Milne. Handbook of Data on Common Organic Compounds. Boca Raton, FL: CRC Press, 1995.
98. C.D. Keefe, J.L. MacDonald. "Optical Constant, Dielectric Constant and Molar Polarizability Spectra of Liquid Hexane Between 4000 and 400 cm^{-1} at 25 °C". J. Mol. Liq. 2005. 121(2-3): 121–126.
99. A.E. Klingbeil, J.B. Jeffries, R.K. Hanson. "Temperature- and Pressure-Dependent Absorption Cross Sections of Gaseous Hydrocarbons at 3.39 μm". Meas. Sci. Technol. 2006. 17(7): 1950–1957.
100. A.E. Klingbeil, J.B. Jeffries, R.K. Hanson. "Temperature-Dependent Mid-IR Absorption Spectra of Gaseous Hydrocarbons". J. Quant. Spectrosc. Radiat. Transfer. 2007. 107(3): 407–420.
101. M.E. Earle, R.G. Pancescu, B. Cosic, et al. "Temperature-Dependent Complex Indices of Refraction for Crystalline $(NH_4)_2SO_4$". J. Phys. Chem. 2006. 110(48): 13022–13028.
102. D.J. Eatough, N.L. Eatough, F. Obeidi, et al. "Continuous Determination of PM2.5 Mass, Including Semi-Volatile Species". Aerosol Sci. Technol. 2001. 34(1): 1–8.
103. R. Subramanian, A.Y. Khlystov, J.C. Cabada, et al. "Positive and Negative Artifacts in Particulate Organic Carbon Measurements with Denuded and Undenuded Sampler Configurations. Aerosol Sci. Technol. 2004. 38: 27–48.
104. J.H. Lee, P.K. Hopke, T.M. Holsen, et al. "Measurements of Fine Particle Mass Concentrations Using Continuous and Integrated Monitors in Eastern US Cities". Aerosol Sci. Technol. 2005. 39(3): 261–275.
105. J.C. Chow, J.G. Watson, D.H. Lowenthal, et al. "Loss of PM2.5 Nitrate from Filter Samples in Central California". J. Air Waste Manag. Assoc. 2005. 55(8): 1158–1168.
106. A.S. Ansari, S.N. Pandis. "Prediction of Multicomponent Inorganic Atmospheric Aerosol Behavior". Atmos. Environ. 1999. 33(5): 745–757.
107. J.S. Chickos, W.E. Acree, J.F. Liebman. "Estimating Solid-Liquid Phase Change Enthalpies and Entropies". J. Phys. Chem. Ref. Data. 1999. 28(6): 1535–1673.
108. J.F. Pankow, W.E. Asher. "Simpol.1: A Simple Group Contribution Method for Predicting Vapor Pressures and Enthalpies of Vaporization of Multifunctional Organic Compounds". Atmos. Chem. Phys. 2008. 8(10): 2773–2796.
109. A. Zuend, C. Marcolli, A.M. Booth, et al. "New and Extended Parameterization of the Thermodynamic Model AIOMFAC: Calculation of Activity Coefficients for Organic-Inorganic Mixtures Containing Carboxyl, Hydroxyl, Carbonyl, Ether, Ester, Alkenyl, Alkyl, and Aromatic Functional Groups". Atmos. Chem. Phys. 2011. 11(17): 9155–9206.

110. National Institute of Standards and Technology (NIST). "Thermodynamics Source Database". In: P.J. Linstrom, W. Mallard, editors. NIST Chemistry Webbook. NIST Standard Reference Database Number 69. Gaithersberg, MD: National Institute of Standards and Technology, 2018. DOI: https://doi.org/10.18434/T4D303.
111. J. Ye, C.A. Gordon, A.W.H. Chan. "Enhancement in Secondary Organic Aerosol Formation in the Presence of Preexisting Organic Particle". Environ. Sci. Technol. 2016. 50(7): 3572–3579.
112. P. Buchwald, N. Bodor. "Molecular Size-Based Model to Describe Simple Organic Liquids". J. Phys. Chem. B. 1998. 102(29): 5715–5726.

Supplementary Material for "Electrospray film deposition for solvent-elimination infrared spectroscopy"

Andrea Arangio, Christophe Delval[†], Giulia Ruggeri[‡],
Nikunj Dudani, Amir Yazdani, Satoshi Takahama

ENAC/IIE Swiss Federal Institute of Technology Lausanne, Lausanne, Switzerland

[†]now at European Patent Office, The Hague, Netherlands

[‡]now at World Health Organization, Geneva, Switzerland

Contents

S1 Calibration equation

In ATR-FTIR, the deposited film can be probed multiple times with evanescent waves generated from each reflection at the interface between IRE and the sample. The resulting reflectance $R = (1 - \alpha d_e)^N$ for N reflections through a sample is a function of its linear decadic absorption coefficient α,[1] and the effective thickness d_e. A mathematical approximation can be invoked to obtain a corollary to the Lambert law under conditions of weak absorption[2–4] ($\alpha d_e \ll 1$), where the absorbance A derived from the attenuation of radiation through a homogeneous medium is proportional to each of these variables:

$$A = -\log_{10} R \approx N \alpha d_e \ . \tag{S1}$$

d_e characterizes the equivalent path length through the sample that gives the same extinction by transmission measurements, and is approximated as:[2,5]

$$d_e = \frac{n_{21}}{\cos\theta}\int_{z=0}^{d} E^2 dz \quad \text{where} \quad E = E_0 \exp\left(-\frac{z}{d_p}\right) \ . \tag{S2}$$

$n_{21} = n_2/n_1$ is the ratio of the real parts of refractive indices of sample medium (n_2) to IRE (n_1), θ is the incident angle, E^2 is the electric field intensity, E_0 is the amplitude of the field at the IRE-sample interface, d_p is the penetration depth, and z is the distance outward from the surface of the IRE. The electric field is integrated from the surface ($z = 0$) to the sample thickness d. d_p is the e-folding distance (reciprocal of the exponential decay constant) for the evanescent wave and depends on the wavelength $\lambda_1 = \lambda/n_1$ in the IRE:[6]

$$d_p = \frac{\lambda_1}{2\pi\left(\sin^2\theta - n_{21}^2\right)^{1/2}} \ . \tag{S3}$$

In the limit of thick samples (semi-infinite medium, $d \gg d_p$, where the evanescent field E sufficiently decays inside the sample), the integral in Eq. S2 approaches $E_0^2 d_p/2$; prompting an empirical "correction" for ATR spectra to adjust for wavelength dependence (Eq. S3) in cases where comparison against transmission spectra are desired. The thin film approximation can be applied at the opposite extreme when $d \ll d_p$, where the electric field can be treated as a constant $E \approx E_0$.[6] The integral in Eq. S2 then approaches $E_0^2 d$, and the effective penetration depth is directly proportional to the physical thickness of the sample.

For substances in a mixture, the dependence of absorption on concentration c is described by corollary to Beer's law for transmission analysis, typically expressed as a relation through the linear absorption coefficient and molar absorption coefficient ε: $\alpha = \varepsilon c$. The analyte concentration multiplied by the film thickness $c \cdot d$ corresponds to an areal density m/a_N,[7] leading to a linear relation between A and deposited mass m for analyte i:

$$\begin{gathered} A = \sum_i \varepsilon_i' m_i \\ \text{where} \quad \varepsilon_i' = \left(\frac{N}{a_N \cos\theta}\right)\left(n_{21}E_0^2\right)\left(\frac{\varepsilon_i}{M_i}\right) \ . \end{gathered} \tag{S4}$$

The linear absorption coefficient, molar absorption coefficient, and refractive index (k)are related by:[7,8]

$$\varepsilon_i \rho_i / M_i = \alpha_i = 4\pi k_i \tilde{\nu} \log_{10} e \ . \tag{S5}$$

$\tilde{\nu}$ is the wavenumber and ρ is the mass density.

S2 Area coverage

In this section, we provide a mathematical argument that Eq. 4 with N/a_N fixed by the IRE geometry applies even for partial sample coverage along the dimension of beam propagation. The Lambert law for a thin film analyzed by ATR-FTIR is given by:

$$A = N\alpha d_e = N\alpha \frac{n_{21}E_0^2}{\cos\theta} d$$

Consider the placement of a pure substance with volumetric mass density ρ and molar mass M with complete coverage along IRE width W perpendicular to beam. Let the IRE area through which N^* reflections ($N^* = 10$

for our configuration) nominally pass be defined as $a_{N^*} = W \times L$. In a scenario where mass m^* covers the IRE completely, $m^* = \rho W L d^*$ and $N = N^*$. The apparent absorbance is given by

$$A^* = N^* \frac{n_{21} E_0^2}{\cos\theta} \alpha d^* = N^* \frac{n_{21} E_0^2}{\cos\theta} \alpha \frac{m^*}{\rho W L} = \left(N^* \frac{n_{21} E_0^2}{\cos\theta} \frac{\alpha}{\rho\, a_{N^*}} \right) m^* \ .$$

For incomplete lengthwise-IRE coverage of the same mass $m^* = \rho W \ell d$, the film is deposited such that $\ell \leq L$ (area coverage is $W \times \ell$), $d \geq d^*$ (film is thicker), and approximately $N = N^* \ell / L$ reflections pass through the sample. Since $N^*/WL \approx N/W\ell$, the apparent absorbance is remains constant ($A = A^*$) for the same mass loading as long as the thin-film approximation is not violated:

$$A = N \frac{n_{21} E_0^2}{\cos\theta} \alpha d = N^* \frac{\ell}{L} \frac{n_{21} E_0^2}{\cos\theta} \alpha \frac{m^*}{\rho W \ell} = \left(N^* \frac{n_{21} E_0^2}{\cos\theta} \frac{\alpha}{\rho\, a_{N^*}} \right) m^* \ .$$

This conclusion can be extended in a straightforward manner to the Beer-Lambert law by incorporating the concentration dependence on α.

S3 Single cone-jet electrospray theory

In the cone-jet mode, the cone breaks up at the tip, ejecting droplets for which the size distribution depends on the flow rate and the electrical conductivity of the purged solution.[9] Theoretically, the first droplet ejected from the cone-jet break up plays a central rule as its charge density determines the propagation speed of the spray and ultimately, the evaporation efficiency.[10] The radius of the first droplet R_e can be estimated[11] from the geometry of the cone and related parameters that affect its shape such as the flow rate Q, the ratio between the applied voltage V_a and the onset voltage V_o, together with the solution density ρ:

$$r_e = \left(\frac{\rho Q^2}{4\pi^2 \tan\left(\frac{\pi}{2} - \phi_T\right) \left[\left(\frac{V_a}{V_o}\right)^2 - 1 \right]} \right)^{1/3} \tag{S6}$$

ϕ_T is the characteristic Taylor angle (49.3°). Typically, the solvent density is used in place of the solution density ($\rho \approx \rho_s$). The charged droplet moves towards the grounded counter electrode dragged by electrostatic forces while shrinking due to solvent evaporation. The shrinkage causes the charge density to increase drastically and above a critical value q_R, the surface tension is not strong enough to counterbalance the Coulomb repulsion and the droplet bursts forming daughter droplets. The critical charge density q_R at which the disintegration takes place is called the Rayleigh limit and it is given by the following equation[12]:

$$q_R = \left[8\pi^2 \epsilon_0 \gamma_s (2r_e)^3 \right]^{1/2} \tag{S7}$$

The same process takes place also for the daughter droplets in which disintegration leads to the complete separation of solute molecules from the solvent and their deposition on the substrate. If the shrinkage process is limited only by evaporation (a valid approximation for small droplets), the time Δt between the emission of the first droplet and the subsequent disintegration is critical for an effective solvent separation; Δt is function of solvent vapor pressure P_s and temperature T[10]:

$$\Delta t = -\left(\frac{4\rho R T}{\alpha_g v P_s M_s} \right) \Delta r_e \tag{S8}$$

Δr_e is the difference between the initial droplet radius (Eq. S6) and droplet radius at disintegration (Eq. S7). R is the gas constant, M_s is the molar mass of the solvent, α_g is the gas accommodation coefficient, and v is the thermal velocity of the molecules in the gas phase. Depending on experimental conditions, the first fission occurs in the microsecond scale and later fissions at shorter intervals[10]. Δt can be used as a reference parameter to estimate the solute-to-solvent separation conditions when different solvents are compared.

S4 ES-ATR-FTIR device

Figure S1 shows the apparatus developed and used in this work. The voltage applied to the needle is controlled by a motherboard (USB X Series 128 channel - National Instruments) which inputs a voltage between 0 and 10 V to a voltage amplifier (10A12 - UltraVolt, Inc.). The needle position is varied along the long direction of the crystal by a motorized stage (MTS50/M-Z8 - 50mm - Thorlabs, Inc.) anchored on an XYZ stage (PT3 - 25 mm, Thorlabs, Inc.) used for fine vertical and plane positioning. The solution is injected to the needle by means of a stepper motor syringe pump. The instrumentation is kept in a purged chamber.

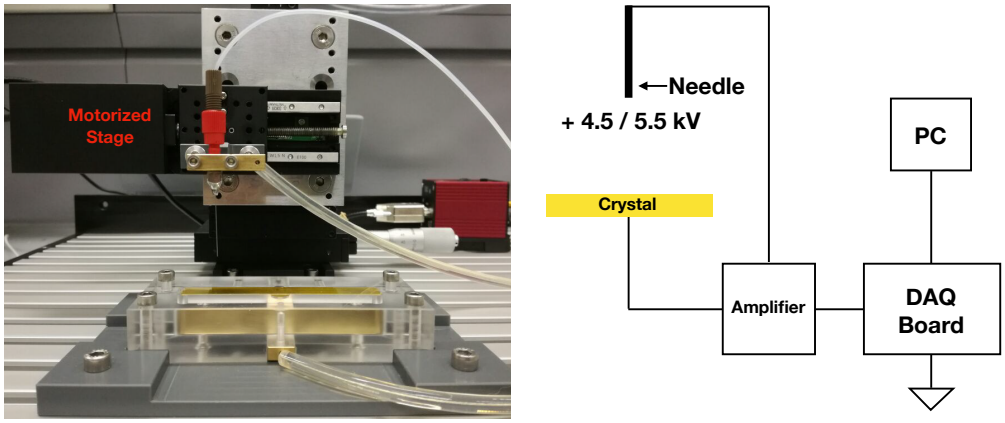

Figure S1: Photograph and diagram of the electrospray apparatus.

S5 Particle morphology

In this section, we characterize the influence of film morphology (i.e., particle formation) on the ATR absorbance spectrum. We compare two scenarios:

- Homogeneous film of thickness d
- Packed monolayer of monodisperse spheres with height $2R$

For a monolayer comprised of monodisperse spheres, let us assume an optimal compact (hexagonal) circle packing deposition. In two dimensions, the packing density η_h is:

$$\eta_h = \frac{\pi\sqrt{3}}{6} \approx 0.91$$

Let the areal density η_R scale with vertical distance z according to the projected area of a single sphere:

$$\eta_R(z) = \eta_h f_R(z) \quad \text{where} \quad f_R(z) = \frac{\pi[R^2 - (R-z)^2]}{\pi R^2} = \left[1 - \frac{(R-z)^2}{R^2}\right] .$$

A substance deposited as a packed monolayer of spheres would have a height $2R = 3d/2\eta_h$ ($\approx 1.7d$) greater than the same mass deposited over a homogeneous film of height d. This result can be obtained by mass

balance (with mass density ρ):

$$\begin{aligned}\int_0^d \rho dz &= \int_0^{2R} \rho\,\eta_R(z) dz \\ \rho\, d &= \rho\,\eta_h \int_0^{2R} \left[1 - \frac{(R-z)^2}{R^2}\right] dz \\ d &= \frac{4}{3}\eta_h R \;\; (\approx 1.2R)\end{aligned} \tag{S9}$$

The electric field of the evanescent wave that diffuse in the sample decays as a function of z and $E(z)$ is given by Eqs. S2 and S3. In the thin-film approximation with film thickness d,

$$\lim_{d\to 0} \int_0^d E_0^2 \exp\left(-2z/d_p\right) dz \to E_0^2 d\ .$$

The apparent absorbance of a homogeneous film and packed sphere monolayer relative to that for which the thin-film appoximation applies is given by:

$$\begin{aligned}\text{Homogeneous film} \quad & \frac{\int_0^d \exp\left(-2z/d_p\right)\, dz}{d} \\ \text{Packed sphere monolayer} \quad & \frac{\int_0^{2R=3d/2\eta_h} \exp\left(-2z/d_p\right) \eta_R(z)\, dz}{d}\ .\end{aligned} \tag{S10}$$

Calculations are shown in Figure S2.

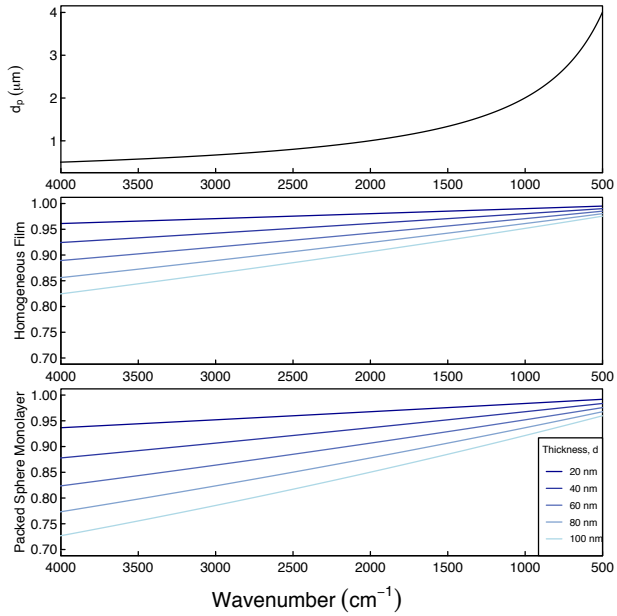

Figure S2: Calculated ratios of expected absorbance relative to wavelength-independent absorbance. Parameters used for calculations: $\theta = 45°$, $n_1 = 2.4$ (ZnSe), $n_2 = 1.5$.

The wavenumber-dependence and= magnitude of discrepancy between transmission-mode and electrosprayed ammonium nitrate spectra suggests that the difference could be due to particle deposition in the ES. Therefore, Eq. S10 is used together with Eq. S9 to estimate an effective particle diameter ($2R$) for electrosprayed

ammonium nitrate by an iterative search of R that leads to the observed magnitude of discrepancy with the transmission-mode spectra. This calculation is repeated for masses of ammonium nitrate accumulated on the IRE by stacking experiments (Figure S3). The analysis indicates that larger particles result from increases in the mass deposition. Even below 5 µg of loading, the particle size is estimated to be greater than 100 nm, with particles generated upon deposition of about 10 µg have estimated diameters of about 200 nm.

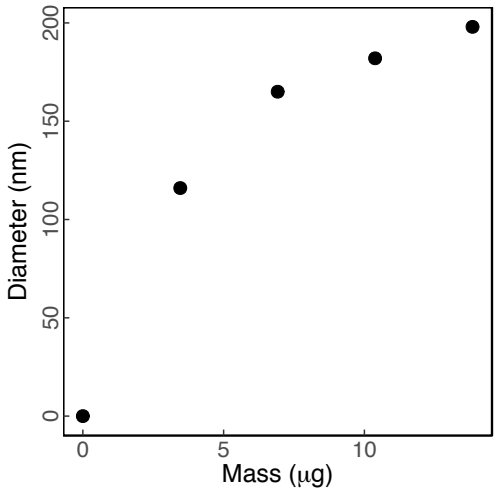

Figure S3: Estimated equivalent diameter of ammonium nitrate particles deposited with electrospray.

More generally, the penetration depth for intermediate cases between packed sphere monolayer and thin film can be written with an arbitrary packing density η_0 (e.g., square packing) in place of η_h. In the present case, n_2 was assumed constant for all cases, but porosity (density) of the substance will affect its value according to effective medium theory. Furthermore, these equations are not valid beyond the point that the length scale of heterogeneities (either $2R$ or pores of air) approach IR wavelengths, as this invalidates the possibility to consider the packed monolayer as a film with a single, refractive index by the effective medium approximation.

S6 Limit of detection

The limit of detection (LOD) was experimentally evaluated by depositing cumulatively 150 ng of docosanol by spraying 100 µL of a solution containing 1.5 µg mL^{-1}. Spectra were recorded using a liquid nitrogen cooled MCT detector. The calibration curve is reported in Figure S4 where the line in blue is the resulting linear regression from which the LOD is calculated as:

$$LOD = \frac{3s_{Y|x}}{b} \text{ where } s_{Y|x} = \sqrt{\frac{\sum(\hat{y}_i - y_i)^2}{n-2}} \ .$$

b is the slope of the regression line and $s_{Y|x}$ is the mean squared error of calibration calculated from the number of samples n, and difference between observed (y_i) and fitted ($\hat{y}_i$) values. The resulting LOD is 48 ng.

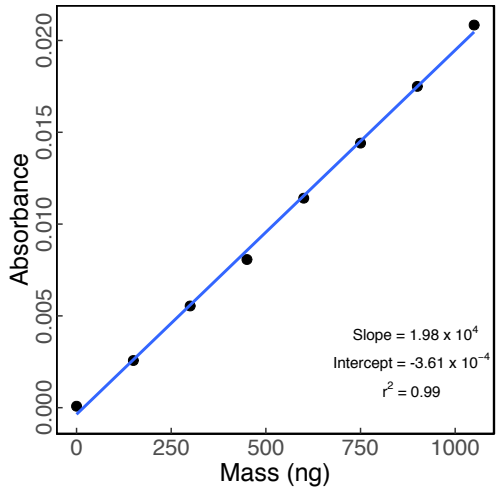

Figure S4: Calibration curve for docosanol ($\nu(-\mathrm{CH}) = 2900\ \mathrm{cm}^{-1}$) in the submicrogram loading range 150 – 1050 ng. Spectra were recorded using a liquid nitrogen cooled MCT detector.

S7 Experimental details - Test set

In the following section, experimental details are given on the test set for both docosanol and ammonium sulfate in Table S1. Additionally, a mixture spectrum of docosanol and ammonium sulfate from the test set is shown together with a spectrum reconstructed from its pure-component contributions (Figure S5).

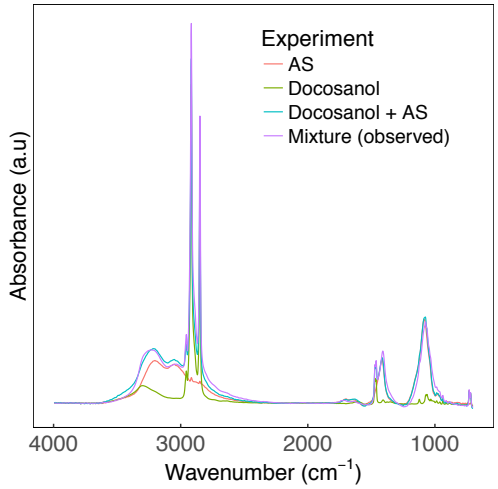

Figure S5: Spectra of pure docosanol (green) and ammonium sulfate (AS in red) from the calibration set, and a mixture spectrum from the test set (violet). Calibration sample spectra of docosanol and ammonium spectra (15.2 and 10.5 µg of loading, respectively) were normalized to unit mass and scaled by the calibration coefficient to obtain equivalent mass loadings in the mixture sample. The sum of the two spectra is shown in blue.

Table S1: Depositions performed to obtain the test dataset for both docosanol and ammonium sulfate shown in Figure 5a and 5b. Mass loadings indicated with (*) refer to depositions performed from a mixture solution of docosanol and ammonium sulfate.

Compound	Mass loading [µg]	Solution concentration [µg/mL]	Volume [mL]	Repetitions
Docosanol	6.4	6.4	1.0	3
Docosanol	11.8	11.8	1.0	3
Docosanol	16.5	16.5	1.0	3
Docosanol	25.2	25.2	1.0	3
Docosanol	34.2	34.2	1.0	3
Docosanol	39.1	39.1	1.0	3
Docosanol	4.6*	15.2	0.3	1
Docosanol	7.6*	15.2	0.5	1
Docosanol	15.2*	15.2	1.0	1
Docosanol	22.9*	15.2	2.0	1
Amm. Sulf.	7.1	59.3	0.12	1
Amm. Sulf.	14.2	59.3	0.24	1
Amm. Sulf.	21.3	59.3	0.36	1
Amm. Sulf.	25.0	25.0	1.0	1
Amm. Sulf.	26.0	26.0	1.0	1
Amm. Sulf.	28.5	28.5	1.0	1
Amm. Sulf.	3.2*	10.6	0.3	1
Amm. Sulf.	5.3*	10.6	0.5	1
Amm. Sulf.	10.6*	10.6	1.0	1
Amm. Sulf.	15.9*	10.6	2.0	1

S8 Volatility

In this section, we provide calculations which show that cis-pinonic acid and docosanol are likely phase-separated after evaporation of methanol solvent, and estimates of vapor pressures that drive the evaporation for initial and final states.

S8.1 Miscibility

In order to understand a priori whether cis-pinonic acid and docosanol produce a homogeneous phase or they separate to form a film deposition with two phases, the Hansen Solubility Parameter (HSP) has been determined using the functional group contribution method.[13] We adapted the notation outlined by Ye et al.[14] in the following description. Within the Hansen solubility framework, the total solubility parameter $\delta_{t,i}$ determines the miscibility between two organic compounds. $\delta_{t,i}$ takes into account three types of intermolecular forces: dispersion forces ($\delta_{d,i}$), dipole-dipole interactions ($\delta_{p,i}$), and hydrogen bonding ($\delta_{hb,i}$). All contributions are combined according to the following equation:

$$\delta_{t,i}^2 = \delta_{d,i}^2 + \delta_{p,i}^2 + \delta_{hb,i}^2 \ .$$

For a particular fucntional group k in a molecule i, its contribution each intermolecular force to the solubility can be calculated from the compiled "molar attraction constant", $F_{d,k}$, $F_{p,k}$, and $E_{hb,k}$[14] according the

following equations:

$$\delta_{d,i} = \sum_k \frac{c_k^i F_{d,k}}{V_k};\ \delta_{p,i} = \frac{\sqrt{\sum_k c_k^i F_{p,k}^2}}{V_k};\ \delta_{hb,i} = \sqrt{\sum_k \frac{c_k^i E_{hb,k}}{V_i}}$$

where c_k^i is the number of the functional group k in the molecule i and V_i is the molecular volume of the compound calculated as a sum of molecular volumes of all functional groups in the molecule. The $\delta_{t,i}$ gives a qualitative estimation of organic miscibility, but each contribution can be used to calculate the Gibbs free energy of the mixing using the Flory-Huggins equation.[15,16] For cis-pinonic acid (cpa) and docosanol (doc):

$$\Delta_{mix}G = \Delta_{mix}H - T\Delta_{mix}S = RT(n_{\text{cpa}} + mn_{\text{doc}})\chi\varphi_{\text{cpa}}\varphi_{\text{doc}} - T[-R(n_{\text{cpa}}\ln\varphi_{\text{cpa}} + n_{\text{doc}}\ln\varphi_{\text{doc}})]$$

where n_{cpa} and n_{doc} are the number of moles of cis-pinonic acid and docosanol respectively, R is the gas constant (8.2×10^{-5} $\text{m}^3\text{atm}\,\text{mol}^{-1}\text{K}^{-1}$), and T is the temperature in Kelvin. Additionally:

$$\varphi_{cpa} = \frac{n_{\text{cpa}}}{n_{\text{cpa}} + mn_{\text{doc}}};\ \varphi_{\text{doc}} = \frac{mn_{\text{doc}}}{n_{\text{cpa}} + mn_{\text{doc}}};\ \text{and}\ m = \frac{V_{\text{doc}}}{V_{\text{cpa}}}\ ,$$

and the parameter χ is the Flory-Huggins parameter defined as:

$$\chi = \frac{V_{\text{cpa}}}{RT}\left[(\delta_{d,\text{cpa}} - \delta_{d,\text{doc}})^2 + \frac{1}{4}(\delta_{p,\text{cpa}} - \delta_{p,\text{doc}})^2 + \frac{1}{4}(\delta_{hb,\text{cpa}} - \delta_{hb,\text{doc}})^2\right]\ .$$

In the experiments reported in this work, $n_{\text{cpa}} = 8.15 \times 10^{-8}$ mol, $n_{\text{doc}} = 4.61 \times 10^{-8}$ mol, and $T = 296.15$ K. The resulting Gibbs free energy of mixing is $\Delta_{mix}G = 2.4 \times 10^{-5}$ J, indicating slighlty unfavorable mixing conditions.

S8.2 Vapor pressure estimation

Considering concentrations at two extremes: that of the bulk solution and final deposited state, we calculate differences in equilibrium vapor pressure of the substances (Table S2) that drives the rate of mass transfer. The temperature dependencies are shown in Figure S6. Calculations are shown below.

Table S2: Thermodynamic properties. "soln" indicates bulk solution composition. x is the mole fraction and γ is the activity coefficient. p denotes the pressure for cis-pinonic acid (cpa) and K_p is the dissociation constant for ammonium nitrate (AN). [*] liquid mixture with docosanol is calculated for comparison.

		binary mixture			tertiary mixture		
	form	x	γ or γ^2	p or K_p	x	γ or γ^2	p or K_p
cpa	soln	3.3×10^{-6}	3.9	$1.3 \times 10^{-5} p^0_{\text{cpa}}$	3.3×10^{-6}	3.9	$1.3 \times 10^{-5} p^0_{\text{cpa}}$
	solute[*]			p^0_{cpa}	6.4×10^{-1}	1.4	$0.9\, p^0_{\text{cpa}}$
AN	soln	5.4×10^{-6}	4.3	$1.3 \times 10^{-10} K_{\text{AN(aq)}}$	NH_4^+=1.2×10^{-5} NO_3^-=5.4×10^{-6}	4.1	$2.7 \times 10^{-10} K_{\text{AN(aq)}}$
	solute			$K_{\text{AN(s)}}$			$K_{\text{AN(s)}}$

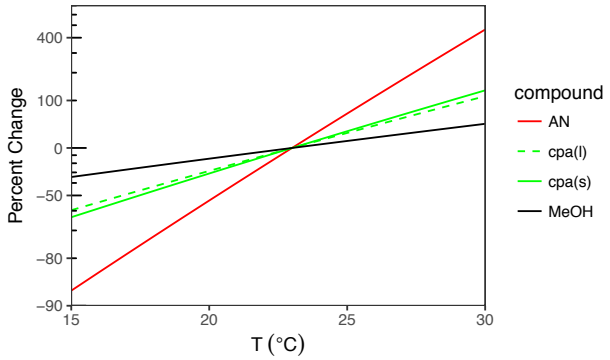

Figure S6: Percent change in vapor pressure with respect to 23 °C, which is the nominal temperature of current experiments. (Note logarithmic y-axis scale.) The nominal phase of pure cis-pinonic acid at room temperature is solid, but liquid-phase vapor pressures for cis-pinonic acid are also shown for reference as environmental organic compound mixtures can often be anticipated exist in non-solid phases.[17,18]

Organic compounds [cis-pinonic acid (cpa) and methanol (MeOH)]. The gas-particle partitioning process of cpa and methanol can be written as reversible reactions:

$$\begin{aligned} \mathrm{cpa}_{(\mathrm{s})} &\leftrightharpoons \mathrm{cpa}_{(\mathrm{g})} \\ \mathrm{cpa}_{(\mathrm{l})} &\leftrightharpoons \mathrm{cpa}_{(\mathrm{g})} \\ \mathrm{MeOH}_{(\mathrm{l})} &\leftrightharpoons \mathrm{MeOH}_{(\mathrm{g})} \end{aligned}$$

The phase state of cpa is solid at room temperature (23 °C in our experiments). As shown in the previous section, cpa is likely phase-separated from docosanol at these conditions. However, given the larger range of compounds with which cpa can be mixed in environmental solutions, we consider the vapor pressure of cpa in both the solid phase and vapor phase. Only the liquid phase for MeOH is considered. The equilibrium constants[19] K_i are equal to the pure component vapor pressures for solid or subcooled liquid (ideal solution reference):

$$\begin{aligned} K_{\mathrm{cpa(s)}} &= p^0_{\mathrm{cpa(s)}} \\ K_{i(\mathrm{l})} &= p^0_{i(\mathrm{l})} = \frac{p_i}{\gamma_i x_i} \ . \end{aligned}$$

x is the mole fraction and γ is the activity coefficient, and p^0 is the pure-component vapor pressure. Equilibrium vapor pressures are given as:

$$\begin{aligned} p_{\mathrm{cpa(s)}} &= K_{\mathrm{cpa(s)}} \\ p_{i(\mathrm{l})} &= K_{i(\mathrm{l})} \gamma_i x_i \ . \end{aligned}$$

$p^0_{\mathrm{cpa(l)}}(T = 296.15\,\mathrm{K}) = 1.1 \times 10^{-7}\,\mathrm{atm}$ is calculated with the group contribution model, SIMPOL.1[20]. $p^0_{\mathrm{cpa(s)}}(T = 296.15\,\mathrm{K}) = 0.39\, p^0_{\mathrm{cpa(l)}} = 4.3 \times 10^{-8}\,\mathrm{atm}$ is estimated from the following equations[21,22] and values in Table S3. Terms that should be considered more generally but not specifically relevant for cis-

pinonic acid are denoted in $\{\cdot\}$.

$$p^0_{\mathrm{cpa(s)}}(T) = p^0_{\mathrm{cpa(l)}}(T) \exp\left[\frac{\Delta_{fus}S^m_{\mathrm{cpa}}}{R}\left(1 - \frac{T_{m,\mathrm{cpa}}}{T}\right)\right]$$

$$\Delta_{fus}S^m_{\mathrm{cpa}} = \Delta_{fus}S_{\mathrm{aah}} + \Delta_{fus}S_{\mathrm{ring}} + \Delta_{fus}S_{\mathrm{corr}} + \Delta_{fus}S_{\mathrm{groups}}$$

$$\Delta_{fus}S_{\mathrm{aah}} = \sum_i n_i G_i + n_{\mathrm{CH_2}} C_{\mathrm{CH_2}} G_{\mathrm{CH_2}} \tag{S11}$$

$$\Delta_{fus}S_{\mathrm{ring}} = 33.4 + 3.7(n-3) \tag{S12}$$

$$\Delta_{fus}S_{\mathrm{corr}} = \sum_i n_i G_i + \{\mathrm{CH_2\ group\ terms}\} \tag{S13}$$

$$\Delta_{fus}S_{\mathrm{groups}} = \sum_i n_i C_i G_i + \{\mathrm{total\ substitution\ terms}\} \tag{S14}$$

The value of $\Delta_{fus}S^m_{\mathrm{cpa}}$ is calculated to be $52.4\,\mathrm{J\,mol^{-1}\,K^{-1}}$. The Clausius-Clapeyron equation[23] is used for estimating the change in vapor pressure ($T_0 = 296.15\,\mathrm{K}$):

$$p^0_{\mathrm{cpa(s)}}(T) = p^0_{\mathrm{cpa(s)}}(T_{m,\mathrm{cpa}}) \exp\left[-\frac{\Delta_{\mathrm{sub}}H^m_{\mathrm{cpa}}}{R}\left(\frac{1}{T} - \frac{1}{T_{m,\mathrm{cpa}}}\right)\right]$$

$$p^0_{i(\mathrm{l})}(T) = p^0_{i(\mathrm{l})}(T_0) \exp\left[-\frac{\Delta_{\mathrm{vap}}H^0_i}{R}\left(\frac{1}{T} - \frac{1}{T_0}\right)\right] .$$

The heat of sublimation is calculated as $\Delta_{sub}H^m_{\mathrm{cpa}} = \Delta_{fus}H^m_{\mathrm{cpa}} + \Delta_{vap}H^m_{\mathrm{cpa}}$ where $\Delta_{fus}H^m_{\mathrm{cpa}} = \Delta_{fus}S^m_{\mathrm{cpa}}T_{m,\mathrm{cpa}}$. $\Delta_{vap}H_{\mathrm{cpa}}$ is calculated by the SIMPOL.1 model and thermodynamic data is taken from the NIST Chemistry Webbook[24] for MeOH.

Table S3: Parameter values applicable for cpa taken from Chikos et al.[21] Units of G are $\mathrm{J\,mol^{-1}\,K^{-1}}$. $T_{m,\mathrm{cpa}} = 67.85\,^{\circ}\mathrm{C}$ for cpa.[25]

Eq.	Group	n	Parameters
(S11)	primary sp^3 (CH_3)	3	$G = 17.6$
	secondary sp^3 (CH_2)	2	$G = 7.1$, $C_{\mathrm{CH_2}} = 1$
	tertiary sp^3 (CH)	1	$G = -16.4$
(S12)	ring	1	none
(S13)	cyclic tertiary sp^3 (CH(R))	1	$G = -14.7$
	cyclic quarternary sp^3 ($C(R)_2$)	1	$G = -34.6$
(S14)	ketone (C=O)	1	$G = 4.6$
	carboxylic acid (COOH)	1	$G = 13.4$

Ammonium nitrate (AN). Gas-particle partitioning of solid or aqueous ammonium nitrate can be written:[26]

$$\mathrm{NH_4NO_{3(s)}} \leftrightharpoons \mathrm{NH_{3(g)}} + \mathrm{HNO_{3(g)}}$$

$$\mathrm{NH_4^+{}_{(aq)}} + \mathrm{HNO_3^-{}_{(aq)}} \leftrightharpoons \mathrm{NH_{3(g)}} + \mathrm{HNO_{3(g)}} .$$

For ammonium nitrate in water, the volatilization is controlled by the acid-base reaction involving ammonia and nitric acid. The equilibrium constants for these processes are given by:

$$K_{\mathrm{AN(s)}} = p_{\mathrm{NH_3}} p_{\mathrm{HNO_3}} = \exp\left(-\frac{\Delta_f G_{\mathrm{NH_3}} + \Delta_f G_{\mathrm{HNO_3}} - \Delta_f G_{\mathrm{NH_4NO_3}}}{RT}\right)$$

$$K_{\mathrm{AN(aq)}} = \frac{p_{\mathrm{NH_3}} p_{\mathrm{HNO_3}}}{\gamma^2_{\mathrm{NH_4NO_3}} x_{\mathrm{NH_4}^+} x_{\mathrm{NO_3}^-}} = \exp\left(-\frac{\Delta_f G_{\mathrm{NH_3}} + \Delta_f G_{\mathrm{HNO_3}} - \Delta_f G_{\mathrm{NH_4}^+} - \Delta_f G_{\mathrm{NO_3}^-}}{RT}\right)$$

with $\gamma^2_{\mathrm{NH_4NO_3}}$ is the mean mixed activity coefficient and follows the ideal-dilute solution reference for solutes. The temperature dependence $\Delta_f G_i = \Delta_f G_i(T)$ is calculated by:

$$\Delta_f G_i(T) = T\left[\frac{\Delta_f G_i^0}{T_0} + \Delta_f H_i^0\left(\frac{1}{T} - \frac{1}{T_0}\right) + c_{p,i}\left(\ln\frac{T_0}{T} - \frac{T_0}{T} + 1\right)\right]$$

with values for $\Delta_f G_i^0, \Delta_f H_i^0, c_{p,i}$ correspond to $T_0 = 298.15\,\mathrm{K}$.[27] The dissociation constants $K_p = p_{\mathrm{NH_3}} p_{\mathrm{HNO_3}}$ are given by:

$$K_{p(\mathrm{s})} = K_{\mathrm{AN(s)}}$$
$$K_{p(\mathrm{aq})} = K_{\mathrm{AN(aq)}} \gamma^2_{\mathrm{NH_4NO_3}} x_{\mathrm{NH_4}^+} x_{\mathrm{NO_3}^-}$$

We obtain $K_{\mathrm{AN(s)}}(T = 296.15\,\mathrm{K}) = 34.79\,\mathrm{ppb}^2$ and $K_{\mathrm{AN(aq)}}(T = 296.15\,\mathrm{K}) = 2.51\,\mathrm{ppb}^2$. While the reported relative humidity (RH) at which aqueous ammonium nitrate crystallizes can be as low as 0%,[28–30] Wu et al.[31] observed solid ammonium nitrate formation at approximately 10% RH. That water absorption bands are not detected in our spectra does not rule out the possibility that ammonium nitrate is not fully crystallized after deposition, we have assumed that the deposited ammonium nitrate is solid for the purposes of this comparison.

References

1. IUPAC. IUPAC compendium of chemical terminology: Gold book, 2009. URL http://goldbook.iupac.org. DOI: 10.1351/goldbook.
2. Kortüm G, Braun W and Herzog G. *Principles and Techniques of Diffuse-Reflectance Spectroscopy*, volume 2. 1963.
3. Milosevic M. *Internal reflection and ATR spectroscopy.* Chemical anaysis, John Wiley & Sons, Inc., 2012. ISBN 978-0-470-27832-1.
4. Woods DA and Bain CD. Total internal reflection spectroscopy for studying soft matter. *Soft Matter* 2014; 10(8): 1071. DOI:10.1039/c3sm52817k.
5. Wendlandt HG and Hecht WWM. *Reflectance Spectroscopy.* Interscience Publishers, 1966. ISBN 978-0-470-93363-3.
6. Harrick NJ. *Internal reflection spectroscopy.* Harrick Scientific Corp, 1967. ISBN 978-0-933946-13-2.
7. Adamson AW. *A Textbook of Physical Chemistry.* 2nd ed. Academic Press, 1979. ISBN 978-0-12-044262-1.
8. Ramer G and Lendl B. Attenuated total reflection Fourier transform infrared spectroscopy. In Meyers RA (ed.) *Encyclopedia of Analytical Chemistry.* John Wiley & Sons, Ltd, 2006. DOI:10.1002/9780470027318.a9287/abstract.

9. Chen DR, Pui DY and Kaufman SL. Electrospraying of conducting liquids for monodisperse aerosol generation in the 4 nm to 1.8 μm diameter range. *Journal of Aerosol Science* 1995; 26(6): 963–977. DOI:10.1016/0021-8502(95)00027-a.

10. Tang L and Kebarle P. Dependence of ion intensity in electrospray mass spectrometry on the concentration of the analytes in the electrosprayed solution. *Analytical Chemistry* 1993; 65(24): 3654–3668.

11. Wilm MS and Mann M. Electrospray and taylor-cone theory, dole's beam of macromolecules at last? *International Journal of Mass Spectrometry and Ion Processes* 1994; 136(2): 167–180.

12. Gomez A and Tang K. Charge and fission of droplets in electrostatic sprays. *Physics of Fluids* 1994; 6(1): 404–414. DOI:10.1063/1.868037.

13. Krevelen DWV. *Properties of Polymers: Their Correlation with Chemical Structure*. Elsevier Science Ltd, 1976. ISBN 0444414673.

14. Ye J, Gordon CA and Chan AWH. Enhancement in secondary organic aerosol formation in the presence of preexisting organic particle. *Environmental Science & Technology* 2016; 50(7): 3572–3579. DOI: 10.1021/acs.est.5b05512.

15. Flory PJ and Rehner J. Statistical mechanics of cross-linked polymer networks II. swelling. *The Journal of Chemical Physics* 1943; 11(11): 521–526. DOI:10.1063/1.1723792.

16. Blanks RF and Prausnitz JM. Thermodynamics of polymer solubility in polar and nonpolar systems. *Industrial & Engineering Chemistry Fundamentals* 1964; 3(1): 1–8. DOI:10.1021/i160009a001.

17. Marcolli C, Luo BP and Peter T. Mixing of the organic aerosol fractions: Liquids as the thermodynamically stable phases. *Journal of Physical Chemistry A* 2004; 108(12): 2216–2224. DOI:10.1021/jp036080l.

18. Koop T, Bookhold J, Shiraiwa M et al. Glass transition and phase state of organic compounds: dependency on molecular properties and implications for secondary organic aerosols in the atmosphere. *Physical Chemistry Chemical Physics* 2011; 13(43): 19238–19255. DOI:10.1039/c1cp22617g.

19. Denbigh K. *The Principles of Chemical Equilibrium*. Cambridge University Press, Cambridge, UK, 1981.

20. Pankow JF and Asher WE. Simpol.1: a simple group contribution method for predicting vapor pressures and enthalpies of vaporization of multifunctional organic compounds. *Atmospheric Chemistry and Physics* 2008; 8(10): 2773–2796. DOI:10.5194/acp-8-2773-2008.

21. Chickos JS, Acree WE and Liebman JF. Estimating solid–liquid phase change enthalpies and entropies. *Journal of Physical and Chemical Reference Data* 1999; 28(6): 1535–1673. DOI:10.1063/1.556045.

22. Lei YD, Chankalal R, Chan A et al. Supercooled liquid vapor pressures of the polycyclic aromatic hydrocarbons. *Journal of Chemical & Engineering Data* 2002; 47(4): 801–806. DOI:10.1021/je0155148.

23. Schwarzenbach RP, Gschwend PM and Imboden DM. *Environmental Organic Chemistry*. 2nd ed. John Wiley & Sons, 2002.

24. Thermodynamics Research Center M NIST Boulder Laboratories. Thermodynamics source database. In Linstrom P and Mallard W (eds.) *NIST Chemistry WebBook, NIST Standard Reference Database Number 69*. National Institute of Standards and Technology, 2018. DOI:10.18434/T4D303.

25. Bradley JC, Lang A and Williams A. Jean-Claude Bradley Double Plus Good (Highly Curated and Validated) Melting Point Dataset. Technical report, 2014. DOI:10.6084/m9.figshare.1031638.v1.

26. Seinfeld J and Pandis S. *Atmospheric Chemistry and Physics: From Air Pollution to Climate Change*. 3rd ed. New York, NY: John Wiley & Sons, 2016. ISBN 9781119221166.

27. Ansari AS and Pandis SN. Prediction of multicomponent inorganic atmospheric aerosol behavior. *Atmospheric Environment* 1999; 33(5): 745–757.

28. Richardson C and Hightower R. Evaporation of ammonium nitrate particles. *Atmospheric Environment (1967)* 1987; 21(4): 971 – 975. DOI:https://doi.org/10.1016/0004-6981(87)90092-8.

29. Lightstone JM, Onasch TB, Imre D et al. Deliquescence, efflorescence, and water activity in ammonium nitrate and mixed ammonium nitrate/succinic acid microparticles. *The Journal of Physical Chemistry A* 2000; 104(41): 9337–9346. DOI:10.1021/jp002137h.

30. Martin ST, Schlenker JC, Malinowski A et al. Crystallization of atmospheric sulfate-nitrate-ammonium particles. *Geophysical Research Letters* 2003; 30(21): 2102. DOI:10.1029/2003GL017930.

31. Wu HB, Chan MN and Chan CK. Ftir characterization of polymorphic transformation of ammonium nitrate. *Aerosol Science and Technology* 2007; 41(6): 581–588. DOI:10.1080/02786820701272038.